International Tables for Crystallography (2018). Vol. H, Chapter 3.6, pp. 288–303.

3.6. Whole powder pattern modelling: microstructure determination from powder diffraction data

M. Leoni

3.6.1. Introduction

X-ray diffraction is a very simple technique, but is one of the most flexible and powerful tools for the analysis of materials. The diffraction pattern carries information about the atomic arrangement and motion at both the short and the long range; for nanostructured materials this means that a single technique can simultaneously provide structural and microstructural information.

Microstructure analysis *via* X-ray powder diffraction (XRD), often termed line-profile analysis (LPA), is mostly performed through the Scherrer (1918) formula. Just a few years after the discovery of X-ray diffraction, Scherrer derived a very simple relationship between the width of the diffraction peaks and the size of the so-called *Kristallchen* (translated as crystallites), the coherently scattering (nanocrystalline) domains composing the colloids that he was studying (the formula is rewritten here using an updated notation):

$$\langle D \rangle = \frac{K_w \lambda}{\mathrm{FWHM}_{hkl} \cos \theta_{hkl}}. \qquad (3.6.1)$$

The calculation of an 'average size' $\langle D \rangle$ is therefore immediate once the position and full-width at half-maximum of a peak ($2\theta_{hkl}$ and FWHM_{hkl}, respectively), measured with X-rays of wavelength λ, are available. The constant K_w (the Scherrer constant) carries information on the shape of the domains and has an order of magnitude of 1. Values of the Scherrer constant can be found in the literature for both isotropic and anisotropic shapes (in the latter case leading to different sizes for different reflections *hkl*): Table 3.6.1 contains the data of Langford & Wilson (1978) for common domain shapes. An elegant derivation of the Scherrer formula can be found in the work of Patterson (1939) and Warren (1990); a summary is also presented in Chapter 5.1.

Its simple mathematical nature is probably the main reason for the widespread (ab)use of equation (3.6.1). Simple, in fact, does not mean accurate.

The Scherrer formula and its variants are based on strong assumptions about the peak shape. In the original derivation [equation (3.6.1)] the peak was assumed to be Gaussian (see Appendix A3.6.1 for the definition of a unit-area Gaussian); in subsequent derivations, the peak-shape information is lost, as the peak is transformed into an equivalent rectangle *via* the use of the integral breadth (IB) $\beta = A/I$, where A and I are the area and the maximum intensity of the peak, respectively (see Table 3.6.1 for the corresponding Scherrer constant values). Together with this, we should consider that the size of the domains in a real specimen is always disperse; it can be easily proven that the quantity $\langle D \rangle$, which is called the 'average size' or 'mean size', is actually not the mean (first moment) of the size distribution, but is related to its third moment (*i.e.* it is volume-weighted). If we add that the finite size of the domains is not the only source of peak broadening, we immediately see where the abuse of the Scherrer formula can lie.

Table 3.6.1
Scherrer constants (K_w and K_β) for various domain shapes (Langford & Wilson, 1978)

Shape	K_w (FWHM)	K_β (integral breadth)
Sphere	0.89	1.07
Cube	0.83–0.91	1.00–1.16
Tetrahedron	0.73–1.03	0.94–1.39
Octahedron	0.82–0.94	1.04–1.14

To try to sort some of those issues out, Williamson & Hall (1953) proposed plotting the FWHM (or the IB) *versus* the reciprocal of the lattice spacing ($d^*_{hkl} = 1/d_{hkl} = 2 \sin \theta_{hkl}/\lambda$). For spherical domains (*i.e.* size independent of the direction), a horizontal line is expected. An anisotropic shape would cause a scattering of the points, whereas other sources of broadening might also change the slope. Following the findings of Stokes & Wilson (1944), Williamson and Hall proposed writing the integral breadth in reciprocal space (reciprocal-space variable d^*) as a combination of the Scherrer formula with the differential of Bragg's law:

$$\beta(d^*) = \frac{K_\beta}{\langle D \rangle} + 2ed^*. \qquad (3.6.2)$$

Equation (3.6.2) describes a line for which the intercept (extrapolation of the integral breadth to the origin of the reciprocal space, *i.e.* to $d \rightarrow \infty$) is related to the reciprocal of the Scherrer size, and the slope parameter e accounts for the distribution of local strain inside the domains. For a Gaussian distribution of this local strain, the root-mean strain (also known as microstrain) $\langle \varepsilon^2 \rangle^{1/2} = e\sqrt{2/\pi}$ can be obtained. The microstrain, which is mostly caused by the presence of imperfections, is often quoted together with the average size.

Even though the Williamson–Hall idea is straightforward, there is no physical reason why the two terms in equation (3.6.2) should be added: the only case where breadths are additive is when the peaks are Lorentzian (see Appendix A3.6.1 for the definition of a unit-area Lorentzian). The Williamson–Hall equation is therefore valid for Lorentzian peaks and under the condition that both the size and strain contributions are Lorentzian as well. We therefore immediately envisage a problem here, as the size contribution, described by the Scherrer equation, was derived in the Gaussian limit. This inconsistency is seldom reported or considered in the literature. The fact that, in the end, the profiles are often highly Lorentzian in character mathematically justifies the separation of a size and a strain term, but dilutes the quantitative meaning of the result.

Modification of the Williamson–Hall approach to remove the inconsistency of the size- and strain-broadening terms has been extensively discussed by Balzar & Popović (1996). Using Voigtians (*i.e.* the convolution of a Gaussian G and a Lorentzian L; see Appendix A3.6.1) to describe a profile, four combinations are possible for the size and strain terms: *L*–*L*, *L*–*G*, *G*–*L* and *G*–*G*. The Williamson–Hall method corresponds to the *L*–*L* case, whereas the combinations involving a Gaussian size term are more compatible with the Scherrer formula. Even in those cases, though, 'The pure-Gauss size-broadened profile is incompatible

with the definitions of surface-weighted domain size and column-length distribution function' (Balzar & Popović, 1996): integral breadth methods are therefore intrinsically limited for the microstructure analysis of real materials. This is in stark contrast to the fact that equation (3.6.2) is used, for example, by a large number of Rietveld refinement codes to describe the observed trend in line-profile broadening (and to perform a rough microstructure analysis). This situation can be improved a little by properly considering at least the anisotropic broadening component, as performed, for example, in the modified Williamson–Hall method (MWH; Ungár & Borbély, 1996; Ungár, 2001; Scardi *et al.*, 2004). The results are more accurate and related to some physical quantities (a dislocation density and a stacking fault probability), but they are still tightly bound to a Voigtian profile approximation.

An alternative to the integral breadth methods was developed by Warren & Averbach (1950, 1952) almost simultaneously with the idea of Williamson and Hall, but took longer to be fully employed owing to the lack of fast computing tools. It is based on the extensive use of Fourier transforms and represents the starting point of modern line-profile analysis techniques. The whole profile carries information on the microstructure, as each point in reciprocal space is related to the Fourier transform of real space (and thus to the size and shape of the domains and also the deviation from perfect three-dimensional periodicity). Each profile also contributes to a better picture of the microstructure, as it samples along a different direction in space.

For decades, these Fourier methods were only used in a very small number of scientific areas; the availability of fast computers and the fast Fourier transform has contributed greatly to their further diffusion. It is, however, only in recent years that the full power of the Fourier approach has been unveiled, with the development of whole-pattern methods and the extension of most models to a wider range of materials.

3.6.2. Fourier methods

3.6.2.1. *Definitions*

In the following, the diffraction peaks for a powder will be described in reciprocal space with reference to the Bragg position $d^*_{\{hkl\}}$ expected for the $\{hkl\}$ reflection family in the absence of any type of defect. The coordinate s, where

$$s = d^* - d^*_{\{hkl\}} = \frac{2}{\lambda}\left(\sin\theta - \sin\theta_{\{hkl\}}\right), \tag{3.6.3}$$

will be employed. Moving from reciprocal to diffraction space ('2θ space') involves a trivial but nonlinear change of variables: peaks that are symmetrical in reciprocal space will become asymmetrical in 2θ space and *vice versa*.

3.6.2.2. *Peak profile and the convolution theorem*

Each peak profile $h(s)$ in a powder diffraction pattern can be described as the convolution of an instrumental profile $g(s)$ with a function $f(s)$ accounting for sample-related effects (microstructure; see, for example, Jones, 1938; Alexander, 1954; Klug & Alexander, 1974; and references therein):

$$h(s) = \int_{-\infty}^{\infty} f(y)g(s-y)\,\mathrm{d}y = f \otimes g(s). \tag{3.6.4}$$

The calculation of the integral in equation (3.6.4) can be simplified through the use of a Fourier transform (FT). In fact, the convolution theorem states that the FT of a convolution is the product of the Fourier transforms of the functions to be folded:

$$\mathcal{C}(L) = \mathrm{FT}[h(s)] = \mathrm{FT}[f(s)] \times \mathrm{FT}[g(s)]. \tag{3.6.5}$$

In this equation, L is the (real) Fourier variable conjugate to s. The properties of the Fourier transform allow equation (3.6.4) to be rewritten as

$$h(s) = \mathrm{FT}^{-1}[\mathcal{C}(L)] = \mathrm{FT}^{-1}\big[\mathrm{FT}[h(s)]\big] = \mathrm{FT}^{-1}\big[\mathrm{FT}[f(s)]\mathrm{FT}[g(s)]\big]. \tag{3.6.6}$$

This equation is the basis of the Warren–Averbach approach and also of all modern LPA methods.

3.6.2.3. *The Warren–Averbach method and its variations*

The convolution theorem can be employed to disentangle the specimen-related broadening contributions described by $f(s)$. In fact, let us suppose, as in the Williamson–Hall method, that size and microstrain are the only two sources of specimen-related broadening. We call the Fourier transform of the profiles broadened by size and distortion effects only $A^S_{hkl}(L)$ and $A^D_{hkl}(L)$, respectively. As the size and distortion profiles are folded into $f(s)$, the following holds:

$$A(L) = \mathrm{FT}[f(s)] = \mathrm{FT}[h(s)]/\mathrm{FT}[g(s)] = A^S_{hkl}(L)A^D_{hkl}(L). \tag{3.6.7}$$

The separation of the size and distortion terms is straightforward for spherical domains: the size effects for a sphere are independent of the reflection order, whereas those related to distortions (causing the change in the slope of the Williamson–Hall plot) are order-dependent. To describe the distortion term it is convenient to follow the idea of Bertaut (1949*a*,*b*, 1950), considering the specimen as made of columns of cells along the **c** direction. The profile due to distortions is calculated by taking the average phase shift along the column due to the presence of defects. The analytical formula for the distortion term is thus of the type $A^D_{hkl}(L) = \langle\exp(2\pi i L n\varepsilon_L)\rangle$, where $\varepsilon_L = \Delta L/L$ is the average strain along **c** calculated for a correlation distance (*i.e.* Fourier length) L.

As a first-order approximation, the distortion terms give no profile asymmetry; $A^D_{hkl}(L)$ is just a cosine Fourier transform. We can thus expand it as (Warren, 1990)

$$A^D_{hkl}(L) = \langle\cos(2\pi L n\varepsilon_L)\rangle = 1 - 2\pi^2L^2n^2\langle\varepsilon_L^2\rangle. \tag{3.6.8}$$

If we now rewrite equation (3.6.7) on a log scale, taking equation (3.6.8) into account, we obtain

$$\begin{aligned}\ln[A_{hkl}(L)] &= \ln[A^S_{hkl}(L)] + \ln[A^D_{hkl}(L)] \\ &= \ln[A^S_{hkl}(L)] + \ln[1 - 2\pi2L^2n^2\langle\varepsilon_L^2\rangle] \\ &= \ln[A^S_{hkl}(L)] - 2\pi^2L^2n^2\langle\varepsilon_L^2\rangle.\end{aligned} \tag{3.6.9}$$

Equation (3.6.9) represents a line in the variable n^2: the intercepts at increasing L values provide the logarithm of the Fourier size term, whereas the slopes give the microstrain directly (Warren, 1990). From the size coefficients, we can obtain an average size, again following the idea of Bertaut (1949*a*, 1950), related to the properties of the Fourier transform:

$$\langle D\rangle = \left[-\frac{\partial A^S_{hkl}(L)}{\partial L}\bigg|_{L=0}\right]^{-1}. \tag{3.6.10}$$

This average size is thus related to the initial slope of the Fourier coefficients [assuming that they are well behaved, *i.e.* that the tangent is always below the $A^S_{hkl}(L)$ curve].

A long chain of operations is needed to obtain the size and the strain contributions; there is thus a risk that the final result will no longer be compatible with the experimental data. Only a few years after the introduction of this method, Garrod *et al.* (1954) wrote

> Hence, in any attempt to distinguish between particle size or strain broadening from a particular material, the use of the one or the other of these functions [Gaussian and Lorentzian] (together with the appropriate relationship between B, b, and β) involves an intrinsic initial assumption about the cause of the broadening, when the object of the investigation is to discover the cause. Such an assumption must inevitably weight the experimental results, partially at least, in favour of one or the other of the two effects. In this connexion it is therefore perhaps significant that in most previous work on the cause of line broadening from cold-worked metals, those investigators who have used the Warren relationship between B, b, and β have concluded that lattice distortion was the predominant factor, whilst those who have employed the Scherrer correction found that particle size was the main cause. The best procedure in such work therefore is to make no assumptions at all about the shape of the experimental line profiles . . .

This is owing to the fact that a direct connection between the experimental data and the final microstructural result does not really exist in those methods and that the whole information contained in the pattern is not exploited.

3.6.2.4. *Beyond the Warren–Averbach method*

The work of Alexander (see, for example, Alexander, 1954; Klug & Alexander, 1974; and references therein) was definitely pioneering here. Alexander proposed a set of formulae for the synthesis of the instrumental profile, with the aim of obtaining a correction curve to subtract the instrumental contribution to the measured breadth of the profiles (thus improving the accuracy of the size determination). The true power of this idea was not fully exploited, as the Scherrer formula was still used for microstructure analysis. A few decades later, Adler, Houska and Smith (Adler & Houska, 1979; Houska & Smith, 1981) proposed the use of simplified analytical functions to describe the instrument, size and strain broadening and to perform the convolution of the equation numerically *via* Gauss–Legendre quadrature. Rao & Houska (1986) improved the procedure by carrying out part of the integration analytically (for monodisperse spheres). The microstructure parameters are directly obtained from a fit of this numerical peak to the experimental data. The fit partly solves the problem of peak overlap: in traditional methods it is in fact impossible to establish the extent of overlap between the peaks and therefore to correctly extract the area or maximum intensity. The method is a major step forward, but is still related to the Warren–Averbach approach, as just two multiple-order peaks are considered.

Cheary & Coelho (1992, 1994, 1998*a*,*b*) pushed the idea forward with the fundamental parameters approach (FPA). The FPA is based on the intuition of Alexander (1954) and the general idea of the Rietveld (1969) method: the calculation speed is greatly improved to facilitate widespread use. The convolution is performed directly in 2θ space, where instrumental aberrations, which were extensively explored by these researchers, occur. Very simplistic models were employed to describe the broadening due to the specimen; the whole pattern (and therefore all of the measured information) is considered in place of one or more peaks and of the extracted information. For structural analysis and for the Rietveld method, the FPA is a huge step forward, as it allows a more accurate determination of lattice parameters and integrated intensities. Moreover, it enables some line-profile analysis on low-quality patterns or on data affected by strong peak asymmetry.

3.6.2.5. *Whole powder pattern modelling (WPPM)*

The techniques briefly illustrated in the previous section, as well as other alternatives appearing in the literature before the beginning of this century, lack full completeness for quantitative microstructure analysis. The whole powder pattern modelling method attempted to fill this gap. Starting with the same ideas as in Section 3.6.2.1 (*i.e.* peaks as convolution), it uses equations (3.6.5) and (3.6.6) to generate the peaks within a fully convolutional approach. The peak profiles are therefore generated from the Fourier transform of each broadening component; the resulting $h(x)$ function accounts just for the shape of the profile, which in turn can be represented as (Scardi & Leoni, 2002)

$$I_{\{hkl\}}(s) = k(d^*)h(s) = k(d^*) \int_{-\infty}^{\infty} \mathcal{C}(L) \exp(2\pi i L s)\, \mathrm{d}L, \quad (3.6.11)$$

where $k(d^*)$ includes all constant or known functions of d^* (*e.g.* structure factor, Lorentz–polarization factor *etc.*), whereas $\mathcal{C}(L)$ is the Fourier transform of the peak profile. The term k is a function of d^*; it is not necessarily a function of s, as the peak is actually centred in $d^*_{\{hkl\}}$.

Equation (3.6.11) assumes that the broadening sources act on the entire family of symmetry-equivalent reflections $\{hkl\}$ and therefore that a multiplicity term [included in $k(d^*)$] can be used: however, certain types of defects (*e.g.* faults) can act independently on each of the symmetry-equivalent reflections. Equation (3.6.11) then becomes more correctly

$$I_{\{hkl\}}(s) = k(d^*) \sum_{hkl} w_{hkl} I_{hkl}(s_{hkl}) = k(d^*) \sum_{hkl} w_{hkl} I_{hkl}(s - \delta_{hkl}), \quad (3.6.12)$$

where w_{hkl} is a weight function depending on the lattice symmetry and actual broadening source, $s_{hkl} = d^* - (d^*_{\{hkl\}} + \delta_{hkl}) = s - \delta_{hkl}$ is the distance, in reciprocal space, from the centroid of the peak hkl, and δ_{hkl} is the shift from $d^*_{\{hkl\}}$, the Bragg position in the absence of defects. The sum is over independent profile subcomponents selected on the basis of the specific defects (*e.g.* two for the {111} family in f.c.c. when faults are present; selection is based on the value of $|L_0| = |h + k + l|$, *i.e.* 3 or 1).

According to equation (3.6.5), the function $\mathcal{C}(L)$ is the product of the Fourier transforms of the broadening contributions. In a real material, broadening is mostly due to the specific nature of the instrument, to the finite size of the coherently diffracting domain (size effect) and to the presence of defects such as, for example, dislocations and faults (Cheary & Coelho, 1992; van Berkum, 1994; Scardi & Leoni, 2002). Taking these into account,

$$\mathcal{C}(L) = T^{\mathrm{IP}}(L) A^S_{hkl}(L) \langle \exp[2\pi i \psi_{hkl}(L)] \rangle \langle \exp[2\pi i \varphi_{hkl}(L)] \rangle \ldots, \quad (3.6.13)$$

where $T^{\mathrm{IP}}(L)$ and $A^S_{hkl}(L)$ are the FTs of the instrumental and domain-size components, respectively, whereas the terms in angle brackets $\langle\,\rangle$ are average phase factors related to lattice distortions (ψ_{hkl}) and faulting (φ_{hkl}).

Equation (3.6.13) is the core of the WPPM method: as indicated by the ellipsis, any other broadening source can easily be considered by including the corresponding (complex) Fourier transform (*i.e.* the corresponding average phase factor) in equation (3.6.13). Expressions are known for several cases of practical interest (see, for example, Scardi & Leoni, 2002, 2004,

2005; Leoni & Scardi, 2004; Leineweber & Mittemeijer, 2004; van Berkum, 1994; Cheary & Coelho, 1992).

The approach is strictly valid when the broadening sources can be considered as diluted and independent (*i.e.* uncorrelated defects). If this does not apply, then cross-terms should be considered and the whole approach revised. In fact, here we assume that the structure factor can be factored and the lattice is fully periodic in three dimensions: under these conditions, structure (peak intensity) and microstructure (peak shape) can be decoupled as the peak positions can be determined in a straightforward way. Extended defects (*e.g.* faults) cause the appearance of diffuse effects and the displacement of the Bragg peaks: in order to calculate the diffraction pattern, the structure and the microstructure must be simultaneously known (see, for example, Drits & Tchoubar, 1990).

3.6.2.6. *Broadening components*

A brief account is given of the main sources of broadening that can be encountered in practice. An accent will be placed on X-rays, but extension to electrons and neutrons is in most cases straightforward. Concerning electron diffraction, precession data can be used in a straightforward way, whereas for traditional data, containing dynamical effects, further calculations, for example of the intensity, are in principle needed.

3.6.2.6.1. *Instrument*

Each of the components of the diffraction instrument (*i.e.* source, optics, specimen stage, measurement geometry and detector) can have a dramatic impact both on the position and the broadening of the peaks. Axial divergence, for instance, introduces both an asymmetric broadening and an apparent shift of the low-angle peaks. When microstructure (*i.e.* specimen-related effects) is the focus of the analysis, the primary recommendation is to try to limit the instrumental influence. Alternatively, it is preferred to have an instrumental profile (no matter how complex) that can be well described and properly simulated: for instance the profile of an instrument with a $K\alpha_1$ primary monochromator (apparently advantageous) might be hard to model if the $K\alpha_2$ removal is not perfect. This becomes more and more important when the instrumental effects are of the same order of magnitude as the specimen-related broadening.

Two possible paths can be followed when dealing with the instrumental contribution: modelling using the fundamental parameters approach (see, for example, Cheary & Coelho, 1992; Kern & Coelho, 1998) or parameterization of the pattern of an ideal specimen. In the fundamental parameters approach, the geometry of the instrument and the effects of each optical component on the peak profile are described mathematically in 2θ. Most of the formulae for the various optical elements can be found, for example, in the work of Wilson (1963), Klug & Alexander (1974) and Cheary & Coelho (1992, 1994, 1998*a*,*b*). The aberration profiles are folded into the (X-ray) source emission profile (Hölzer *et al.*, 1997; Deutsch *et al.*, 2004) to generate a combined instrumental profile.

When no information on the instrument is available, it is possible to predict the instrumental profile just by using the nominal data for the optical components. It is however advised, whenever possible, to tune the instrumental parameters using the pattern of a line-profile standard [*e.g.* NIST LaB_6 SRM 660(x) series; Cline *et al.*, 2010] showing negligible specimen effects. These instrument-only parameters must then be kept fixed for any subsequent microstructure refinement. It is of paramount importance that all instrumental features are well reproduced when dealing with microstructure effects. Provided that this condition is met, we can therefore employ any arbitrary function to describe the instrumental profile. Thus, as an alternative to FPA, we can either 'learn' the instrumental profile from a standard (Bergmann & Kleeberg, 2001) or use a Voigtian to model it. The Voigtian is particularly convenient as it can be defined directly in L space and thus directly enter the Fourier product of equation (3.6.13).

3.6.2.6.2. *Source emission profile*

For X-rays, the source emission profile at an energy E_l can be well described by a Lorentzian of energy width Γ_l (Hölzer *et al.*, 1997; Deutsch *et al.*, 2004),

$$I_l(E) = \frac{2}{\Gamma_l \pi}\left[1 + 4\left(\frac{E - E_l}{\Gamma_l}\right)^2\right]^{-1}. \tag{3.6.14}$$

As $\mathrm{d}E/E = \mathrm{d}\lambda/\lambda = \mathrm{d}s/s$, the function can also be represented as a function of s:

$$I^{\mathrm{IP}}_{hkl,l}(s, d^*_{hkl}) = \frac{2}{\pi}\frac{E_l}{d^*_{hkl}\Gamma_l}\left[1 + 4\left(\frac{s_{hkl}}{d^*_{hkl}\Gamma_l/E_l}\right)^2\right]^{-1}. \tag{3.6.15}$$

For a laboratory tube emitting simultaneously a set of N_λ wavelengths, we have

$$I^{\mathrm{IP}}_{hkl}(s, d^*_{hkl}) = \sum_{l=1}^{N_\lambda} w_l I^{\mathrm{IP}}_{hkl,l}(s, d^*_{hkl}), \tag{3.6.16}$$

where w_l is the relative intensity of the lth wavelength component (referred, for example, to $w_1 = 1$). The corresponding Fourier transform entering (3.6.13) can be written as

$$\begin{aligned} T^{\mathrm{IP}}(L) &= \sum_{l=1}^{N_\lambda} \exp\left[2\pi i d^*_{hkl}\left(1 - \frac{\Gamma_l}{E_l}\right)L\right]\exp\left(-2\pi s_{hkl}\frac{\Gamma_l}{E_l}L\right) \\ &= \sum_{l=1}^{N_\lambda}\left\{\cos\left[2\pi d^*_{hkl}\left(1 - \frac{\Gamma_l}{E_l}\right)L\right] + i\sin\left[2\pi d^*_{hkl}\left(1 - \frac{\Gamma_l}{E_l}\right)L\right]\right\} \\ &\quad \times \exp\left(-2\pi s_{hkl}\frac{\Gamma_l}{E_l}L\right). \end{aligned} \tag{3.6.17}$$

The complex term in (3.6.17) accounts for the shift of each emission component with respect to the reference one. For more flexibility (for example to consider the non-ideal behaviour of the instrument), we can use a pseudo-Voigt (pV) in place of the Lorentzian in equation (3.6.14).

3.6.2.6.3. *Optical elements*

The equation of Caglioti *et al.* (1958), modified by Rietveld (1969) and originally developed for constant-wavelength neutron diffraction, is frequently employed for parameterization of the instrumental profile. The FWHM and the pV mixing parameter η (replacing the Lorentzian and Gaussian widths of the Voigt) are then parameterized according to functions in $\tan(\theta)$ and θ, respectively (Caglioti *et al.*, 1958; Leoni *et al.*, 1998; Scardi & Leoni, 1999),

$$\mathrm{FWHM}^2 = U\tan^2\theta + V\tan\theta + W, \tag{3.6.18}$$

$$\eta = a + b\theta + c\theta^2. \tag{3.6.19}$$

The parameters of the Fourier transform of a Voigt or pseudo-Voigt are then constrained to those of equations (3.6.18) and

(3.6.19). This is particularly convenient, as the Fourier transform of a Voigtian is analytical. In fact, for the pV case we have

$$T_{\rm pV}^{\rm IP}(L) = (1-k)\exp(-\pi^2\sigma^2L^2/\ln 2) + k\exp(-2\pi\sigma L), \tag{3.6.20}$$

where σ = FWHM/2 and where (Langford & Louër, 1982; Scardi & Leoni, 1999)

$$k = \left[1 + (1-\eta)/\left(\eta\sqrt{\pi\ln 2}\right)\right]^{-1}. \tag{3.6.21}$$

Equation (3.6.18) can be found in the literature in a different form and with additional terms accounting, for example, for size effects: besides forcing a symmetry of the profile in 2θ space, these extra terms are a contradiction as they have nothing to do with the instrument itself.

3.6.2.6.4. *Domain size and shape*

In nanostructured materials, the finite size of the scattering domains is usually the dominant source of line-profile broadening. Actually, when dealing with size, we should consider a size and a shape distribution of the domains. In most cases, one or more distributions of similar objects are considered. For an up-to-date description of issues related to size broadening, see Chapter 5.1. The domain shape is not a property of the material and therefore the use of symmetry constraints [*e.g.* spherical harmonics to describe the shape of the scattering object as in the model of Popa (1998) or as a size extension of Stephens' (1999) work] is not justified in the general case (Nye, 1987). Exceptions, however, exist.

The size-broadening contribution in WPPM follows the ideas of Bertaut (1949*a*,*b*, 1950) and of Stokes & Wilson (1942). Bertaut proposed the division of the domains into columns and the analysis of the independent scattering of these columns. The column-length distribution can always be extracted from the data: more complex models involving given shapes or distributions simply modify the way in which the columns are rearranged. Stokes and Wilson introduced the concept of a *ghost* to calculate the Fourier transform for a given shape: the volume common to a domain of shape c and its ghost, *i.e.* a copy of the same domain displaced by a quantity L along the scattering direction hkl, is proportional to the (size) Fourier transform $A^S_{c,hkl}(L, D)$ for the given domain. The calculation has been already carried out analytically for several simple shapes characterized by a single length parameter (Stokes & Wilson, 1942; Lele & Anantharaman, 1966; Wilson, 1969; Langford & Louër, 1982; Vargas *et al.*, 1983; Grebille & Bérar, 1985; Scardi & Leoni, 2001), and can be performed numerically in the general case (Leonardi *et al.*, 2012). It is possible to relate the Fourier coefficients to the size values obtained from traditional methods. In particular, the area-weighted average size $\langle L\rangle_S$ (Warren–Averbach method) and the volume-weighted average size $\langle L\rangle_V$ (Williamson–Hall method) are obtained as

$$\langle L\rangle_S = -\left[dA^S_c(L,D)/dL\big|_{L=0}\right]^{-1} = D/K_k = -D/H_1, \tag{3.6.22}$$

$$\langle L\rangle_V = [\beta(s)]^{-1} = 2\int_0^{D/K} A^S_c(L,D)\,{\rm d}L = D/K_\beta, \tag{3.6.23}$$

where $\beta(s)$ is the integral breadth and K_k and K_β are the initial slope and integral breadth Scherrer constants, respectively (Langford & Wilson, 1978; Scardi & Leoni, 2001).

The average size might have little physical significance in real cases: the size (and shape) distribution can in fact play a key role in determining both the properties and the diffraction line-profile shapes of the powder under analysis. Fortunately, the Fourier coefficients for the polydisperse case can be easily calculated for any given distribution: the log-normal and the gamma distributions are the most common (and the most flexible). The equations and the corresponding moments are

$$g_l(D) = \frac{1}{D\sigma_l\sqrt{2\pi}}\exp\left[-\frac{(\ln D-\mu_l)^2}{2\sigma_l^2}\right],$$
$$M_{l,n} = \exp\left(n\mu_l + \frac{n^2}{2}\sigma_l^2\right), \tag{3.6.24}$$

$$g_g(D) = \frac{\sigma_p}{\mu_g\Gamma(\sigma_g)}\left(\frac{\sigma_g D}{\mu_g}\right)^{\sigma_g-1}\exp\left(-\frac{\sigma_g D}{\mu_g}\right),$$
$$M_{g,n} = \left(\frac{\mu_g}{\sigma_g}\right)^n\frac{\Gamma(n+\sigma_g)}{\Gamma(\sigma_g)}. \tag{3.6.25}$$

The scattered intensity for the given distribution g_i, and the given shape c, is

$$\begin{aligned} I_{c,hkl}(s) &\propto \frac{\int_0^\infty\left[\int_{L=0}^{D/K_{hkl}} A^S_{c,hkl}(L,D)\exp(2\pi iLs)\,{\rm d}L\right]w(D)\,{\rm d}D}{\int_0^\infty w(D)\,{\rm d}D} \\ &\propto \int_{L=0}^\infty\left[\frac{\int_{D=LK_{hkl}}^\infty A^S_{c,hkl}(L,D)w(D)\,{\rm d}D}{\int_0^\infty w(D)\,{\rm d}D}\right]\exp(2\pi iLs)\,{\rm d}L \\ &\propto \int_{L=0}^\infty A^S_{hkl}(L)\exp(2\pi iLs)\,{\rm d}L, \end{aligned} \tag{3.6.26}$$

where $w(D) = g_i(D)V_c(D)$ and where

$$A^S_{hkl}(L) = \frac{\int_{D=LK_{hkl}}^\infty A^S_{c,hkl}(L,D)w(D)\,{\rm d}D}{\int_0^\infty w(D)\,{\rm d}D}. \tag{3.6.27}$$

With a suitable definition of the Fourier coefficients, the polydisperse case therefore becomes analogous to the monodisperse case. Analytic expressions can be obtained in particular cases. For instance, the Fourier coefficients for the log-normal and gamma distributions (Scardi & Leoni, 2001) are

$$A^S_l(L) = \sum_{n=0}^3 {\rm erfc}\left[\frac{\ln(LK_c)-\mu_l-(3-n)\sigma_l^2}{\sigma_l\sqrt{2}}\right]\frac{M_{l,3-n}}{2M_{l,3}}H_n^cL^n \tag{3.6.28}$$

and

$$A^S_g(L) = \sum_{n=0}^3\left(\frac{\sigma_g}{M_{g,1}}\right)^n\frac{\Gamma[\sigma_g+(3-n),K_cL\sigma_g/M_{g,1}]}{\Gamma(\sigma_g+3)}H_n^cL^n, \tag{3.6.29}$$

respectively, where

$$\Gamma(x,a) = \int_a^\infty y^{x-1}\exp(-y)\,{\rm d}y,$$
$$\Gamma(x) = \Gamma(x,0),$$
$${\rm erfc}(x) = 2\pi^{-1/2}\int_x^\infty\exp(-y^2)\,{\rm d}y,$$

with the definitions already given in equations (3.6.24) and (3.6.25).

The functional forms of equations (3.6.28) and (3.6.29) clearly suggest that the profile for a log-normal distribution of domains (which is frequently encountered in practice) is not Voigtian: all traditional line-profile analysis methods (based on Voigt or pseudo-Voigt functions) are therefore unable to correctly deal with a log-normally dispersed powder.

By analogy to the monodisperse case, it is possible to relate the parameters of the polydisperse system to the size obtained with traditional methods (Warren–Averbach and Williamson–Hall, respectively). The following holds (Krill & Birringer, 1998; Scardi & Leoni, 2001):

$$\langle L\rangle_S = \frac{1}{K_k}\frac{M_{i,3}}{M_{i,2}}, \quad \langle L\rangle_V = \frac{1}{K_\beta}\frac{M_{i,4}}{M_{i,3}}. \tag{3.6.30}$$

Here, it is clear that diffraction does not provide the first moment of the distribution directly: ratios between high-order moments are involved.

Using an analytical expression for the description of a size distribution can help in stabilizing the results (as the size distribution curve is forced to be zero at very small and very large size values). Some doubts can, however, arise as to the physical validity of this forcing. An example is the case of a multimodal system. The traditional LPA techniques are unable to directly deal with multimodal size distributions. In cases where the multimodal character is clear and the various distribution are well behaved (*i.e.* when they can be modelled with analytical functions), the pattern can be usually modelled by considering the material as made of different fractions, each of them characterized by a different size distribution.

A possible alternative has been proposed in the literature: replacing the analytical distribution with a histogram. The ability of this model to fit the experimental data has been demonstrated (Leoni & Scardi, 2004; Matěj *et al.*, 2011); a regularization might be necessary to stabilize the shape and/or smoothness of the size distribution. The quality of the measurement and the availability of models describing all contributions to the peak broadening are in most cases the limiting factors for extensive use of the histogram model: correlations of small sizes with the background and with features such as thermal diffuse scattering (Beyerlein *et al.*, 2012) can in fact occur. So far, this is the only available method for exploring cases where the analytical models are unable to correctly describe the observed broadening.

3.6.2.6.5. *Strain broadening (lattice distortions)*

A local variation of the lattice spacing (due, for example, to the presence of a defect) leads to an average phase term that, in general, is a complex quantity:

$$\begin{aligned}\langle\exp[2\pi i\psi_{hkl}(L)]\rangle &= \langle\cos[(2\pi L d^*_{\{hkl\}}\varepsilon_{\{hkl\}}(L)]\rangle \\ &\quad + i\langle\sin[2\pi L d^*_{\{hkl\}}\varepsilon_{\{hkl\}}(L)]\rangle \\ &= A^D_{\{hkl\}}(L) + iB^D_{\{hkl\}}(L).\end{aligned} \tag{3.6.31}$$

The strain $\varepsilon_{\{hkl\}}(L)$ represents the relative displacement of atoms at a (coherence) distance L along the scattering vector hkl. Knowledge of the actual source of distortion allows the explicit calculation of the various terms (van Berkum, 1994). It is quite customary to assume that the strain is the same for symmetry-equivalent reflections [$\varepsilon_{hkl}(L) = \varepsilon_{\{hkl\}}(L)$]: this is a reasonable hypothesis for a powder, where we assume that any configuration is equally probable.

Traditional LPA methods such as the Warren–Averbach method (Warren & Averbach, 1950, 1952; Warren, 1990) take a first-order MacLaurin expansion of equation (3.6.31) to extract the microstrain contribution from the measured data:

$$A^D_{\{hkl\}}(L) \cong 1 - 2\pi^2 L^2 d^{*2}_{\{hkl\}}\langle\varepsilon^2_{\{hkl\}}(L)\rangle, \tag{3.6.32}$$

$$B^D_{\{hkl\}}(L) \cong -\frac{4}{3}\pi^3 L^3 d^{*3}_{\{hkl\}}\langle\varepsilon^3_{\{hkl\}}(L)\rangle. \tag{3.6.33}$$

The term in equation (3.6.33) would cause peak asymmetry. However, we usually consider only the second-order moment of the strain distribution (*root-mean strain* or *microstrain*) and thus symmetric peaks. Owing to the anisotropy of the elastic properties, the broadening described by equation (3.6.32) is in general anisotropic: an extensive discussion of strain anisotropy and of the order dependence of strain broadening can be found, for example, in Leineweber & Mittemeijer (2010) and Leineweber (2011). It should be stressed that in their original form, traditional line-profile methods are unable to deal with this anisotropy (corrections have been proposed for particular cases, for example, in the so-called modified Williamson–Hall (MWH) and modified Warren–Averbach (MWA) analyses; Ungár & Borbély, 1996).

3.6.2.6.6. *Dislocations*

Dislocations are often the main source of strain broadening. The magnitude of this broadening depends not only on the elastic anisotropy of the material, but also on the relative orientation of the Burgers and diffraction vectors with respect to the dislocation line (Wilkens, 1970*a*,*b*). This problem was analysed in the 1960s by Krivoglaz and Ryaboshapka (Krivoglaz & Ryaboshapka, 1963; Krivoglaz, 1969) and then subsequently reprised and completed by Wilkens (1970*a*,*b*). Further elements have been added to put it into the present form (see, for example, Krivoglaz *et al.*, 1983; Groma *et al.*, 1988; Klimanek & Kuzel, 1988; van Berkum, 1994; Kamminga & Delhez, 2000). For the purpose of WPPM, the distortion Fourier coefficients caused by dislocations can be written as

$$A^D_{\{hkl\}}(L) = \exp[-\tfrac{1}{2}\pi b^2\overline{C}_{\{hkl\}}\rho d^{*^2}_{\{hkl\}}L^2 f(L/R'_e)], \tag{3.6.34}$$

where b is the modulus of the Burgers vector, $\overline{C}_{\{hkl\}}$ is the so-called average contrast factor of the dislocations, ρ is the density of the dislocations and R'_e is an effective outer cutoff radius. Only the low-L trend of equation (3.6.34) is well reproduced by Wilkens' theory: a decaying function $f(L/R'_e)$ has thus been introduced to guarantee a proper convergence to zero of the Fourier coefficients for increasing L. Actually, the function $f^*(\eta)$ is mostly quoted in place of (L/R'_e), where $\eta = (e^{-1/4}/2)L/R'_e$: the multiplicative term can however be dropped, considering that the cutoff radius is an effective value [some discussion of the meaning of the f and f^* functions and of the effective cutoff radius can be found in Scardi & Leoni (2004), Armstrong *et al.* (2006) and Kaganer & Sabelfeld, 2010)].

The most complete definition of $f^*(\eta)$ is from Wilkens (1970*a*,*b*):

$$f^*(\eta) = -\ln\eta + \frac{7}{4} - \ln 2 + \frac{256}{45\pi\eta} + \frac{2}{\pi}\left(1 - \frac{1}{4\eta^2}\right)\int_0^\eta \frac{\arcsin y}{y}\,\mathrm{d}y - \frac{1}{\pi}\left(\frac{769}{180\eta} + \frac{41}{90}\eta + \frac{\eta^3}{45}\right)(1-\eta^2)^{1/2} - \frac{1}{\pi}\left(\frac{11}{12\eta^2} + \frac{7}{2} + \frac{\eta^2}{3}\right)\arcsin\eta + \frac{\eta^2}{6}, \qquad \eta \le 1, \tag{3.6.35}$$

$$f^*(\eta) = \frac{256}{45\pi\eta} - \left(\frac{11}{24} + \frac{1}{4}\ln 2\eta\right)\frac{1}{\eta^2}, \qquad \eta \ge 1. \tag{3.6.36}$$

For $\eta < 1$, the integral in (3.6.35) can be calculated in terms of special functions as

$$\begin{aligned}\int_0^\eta \frac{\arcsin y}{y}\,\mathrm{d}y &= \frac{i}{12}\left\{\pi^2 - 6\arcsin^2\eta - 12i\ln\left[2\eta\left(\eta - i\sqrt{1-\eta^2}\right)\right]\arcsin\eta - 6\mathrm{Li}_2\left(1 - 2\eta^2 + 2i\eta\sqrt{1-\eta^2}\right)\right\}\\ &= \ln(2\eta)\arcsin\eta + \frac{1}{2}\mathrm{Im}\left[\mathrm{Li}_2\left(1 - 2\eta^2 + 2i\eta\sqrt{1-\eta^2}\right)\right]\\ &= \ln(2\eta)\arcsin\eta + \frac{1}{2}\mathrm{Cl}_2(2\arcsin\eta),\end{aligned} \tag{3.6.37}$$

where $\mathrm{Li}_2(z)$ and $\mathrm{Cl}_2(z)$ are the dilogarithm function (Spence's function) and the Clausen integral, respectively:

$$\mathrm{Li}_2(z) = \sum_{k=1}^{\infty} z^k/k^2, \tag{3.6.38}$$

$$\mathrm{Cl}_2(z) = \sum_{k=1}^{\infty} \sin(kz)/z^2 = -\int_0^x \ln[2\sin(t/2)]\,\mathrm{d}t. \tag{3.6.39}$$

The approximation proposed by van Berkum (1994) for (3.6.35) and (3.6.36),

$$f^*(\eta) = \begin{cases} -\ln\eta + \dfrac{7}{4} - \ln 2 + \dfrac{\eta^2}{6} - \dfrac{32\eta^3}{225\pi}, & \eta \le 1 \\ \dfrac{256}{45\pi\eta} - \left(\dfrac{11}{24} + \dfrac{1}{4}\ln 2\eta\right)\dfrac{1}{\eta^2}, & \eta \ge 1, \end{cases} \tag{3.6.40}$$

should not be employed, as the derivative is discontinuous at $\eta = 1$. A simpler approximation, valid over the whole η range, was provided by Kaganer & Sabelfeld (2010):

$$f^*(\eta) = -\ln\left(\frac{\eta}{\eta_0 + \eta}\right). \tag{3.6.41}$$

With $\eta_0 = 2.2$, the results of equation (3.6.41) are similar to those of (3.6.35) and (3.6.36).

Together with dislocation density and outer cutoff radius, a parameter traditionally quoted for the dislocations ensemble is Wilkens' dislocation arrangement parameter $M = R_e\sqrt{\rho}$ (Wilkens, 1970*a*). By combining the information on dislocation screening and dislocation distance, it gives an idea of the interaction of dislocations (strength of the dipole character; Ungár, 2001). A value close to or below unity indicates highly interacting dislocations (for example, dipole configurations or dislocation walls), whereas a large value is typical of a system with randomly dispersed dislocations (weak dipole character).

The anisotropic broadening caused by the presence of dislocations is mainly taken into account by the contrast (or orientation) factor C_{hkl}. The contrast factor depends on the strain field of the dislocation and therefore on the elastic anisotropy and orientation of the scattering vector with respect to the slip system considered. The average of the contrast factor over all equivalent slip systems, $\overline{C}_{hkl}$, is often used in the analysis of powders. The averaging is usually performed under the assumption that all equivalent slip systems are equally populated. The calculation of the contrast factor can be lengthy: full details can be found in the literature (Wilkens, 1970*a*,*b*, 1987; Krivoglaz *et al.*, 1983; Kamminga & Delhez, 2000; Groma *et al.*, 1988; Klimanek & Kuzel, 1988; Kuzel & Klimanek, 1989) for the cubic and hexagonal cases. For a generalization, the reader is referred to the recent work of Martinez-Garcia *et al.* (2007, 2008, 2009). It is possible to show that the contrast factor of a given material has the same functional form as the fourth-order invariant of the Laue class (Popa, 1998; Leoni *et al.*, 2007):

$$\begin{aligned}d^4_{\{hkl\}}C_{\{hkl\}} &= E_1h^4 + E_2k^4 + E_3l^4 + 2(E_4h^2k^2 + E_5k^2l^2 + E_6h^2l^2)\\ &\quad + 4(E_7h^3k + E_8h^3l + E_9k^3h + E_{10}k^3l + E_{11}l^3h + E_{12}l^3k)\\ &\quad + 4(E_{13}h^2kl + E_{14}k^2hl + E_{15}l^2hk).\end{aligned} \tag{3.6.42}$$

In the general case, 15 coefficients are thus needed to describe the strain anisotropy effects. Symmetry reduces the number of independent coefficients: for instance, two coefficients survive in the cubic case, and the average contrast factor is (Stokes & Wilson, 1944; Popa, 1998; Scardi & Leoni, 1999)

$$\overline{C}_{\{hkl\}} = (A + BH) = A + B\frac{h^2k^2 + h^2l^2 + k^2l^2}{(h^2 + k^2 + l^2)^2}. \tag{3.6.43}$$

The values of A and B can be calculated from the elastic constants and slip system according to the literature (Klimanek & Kuzel, 1988; Kuzel & Klimanek, 1989; Martinez-Garcia *et al.*, 2007, 2008, 2009). Excluding the case of $\overline{C}_{\{h00\}} = 0$, the parameterization $\overline{C}_{\{hkl\}} = \overline{C}_{\{h00\}}(1 + qH)$ proposed by Ungár & Tichy (1999) can also be used. Some calculated values for cubic and hexagonal materials can be found in Ungár *et al.* (1999) and Dragomir & Ungár (2002), respectively.

As the calculation of the contrast factor for a dislocation of general character is not trivial, it is customary to evaluate it for the screw and edge case and to refine an effective dislocation character φ (Ungár *et al.*, 1999),

$$\begin{aligned}\overline{C}_{\{hkl\}} &= [\varphi\overline{C}_{E,\{hkl\}} + (1-\varphi)\overline{C}_{S,\{hkl\}}]\\ &= [\varphi A_E + (1-\varphi)A_S] + [\varphi B_E + (1-\varphi)B_S]H,\end{aligned} \tag{3.6.44}$$

where the geometric term H is the same as in equation (3.6.43). Although not completely correct, the approach proposed in equation (3.6.44) allows the case where a mixture of dislocations of varying character are acting on equivalent slip systems to be dealt with. For a proper refinement, however, the active slip systems as well as the contrast factors of the edge and screw dislocations should be known.

It is worth mentioning that the invariant form proposed by Popa (1998) has been reprised by Stephens (1999) to describe the strain-broadening anisotropy, for example, within the Rietveld method: the formula correctly accounts for the relative broadening (*i.e.* for the anisotropy), but it does not give any information on the actual shape of the profiles. This is the major reason

why the Stephens model can be considered as only phenomenological (it captures the trend but not the details): when the source of microstrain broadening is known, we can obtain the functional form of the profile (as proposed, for example, here for dislocations) and the model can become exact.

3.6.2.6.7. *Twin and deformation faults*

Planar defects, *i.e.* a mismatch in the regular stacking of crystallographic planes, are quite frequent in a vast family of technologically important materials and, in some cases, are responsible for their macroscopic properties. In the general case, the analysis of faulting using a Bragg-type method is troublesome. The local change in the structure causes the appearance of diffuse scattering (*i.e.* extra intensity) between the Bragg spots. This can be handled in the single-crystal case (Welberry, 2004), but can be challenging in a powder, where the reciprocal space is rotationally averaged and the (weak) diffuse scattering is lost in the background. The handling of diffuse phenomena is the main difference between the Rietveld (1969) and the pair distribution function (PDF) (Billinge, 2008) methods.

A simple description of the broadening effects of faulting, useful for WPPM, is available only for a restricted class of systems, namely face-centred cubic (f.c.c.) ($Fm\bar{3}m$), body-centred cubic (b.c.c.) ($Im\bar{3}m$) and hexagonal close packed (h.c.p.) ($P6_3/mmc$) lattices. Monatomic metals with f.c.c. (*e.g.* Cu, Ni and Au), h.c.p. (*e.g.* Ti, Co and Zr) and b.c.c. (*e.g.* W and Mo) structures fall into this list. Faulting in the wurtzite structure ($P6_3mc$) leading to a local transformation into sphalerite ($F\bar{4}3m$) can be handled with rules completely analogous to those for the h.c.p./f.c.c. case. The main types of faults in all of these systems are the so-called deformation and twin faults: looking at the planes on the two sides of the faulting, a deformation fault appears as a shear, whereas twinning causes a mirroring of the atomic positions. The effect of these defects can be modelled using recurrence equations for the stacking. Initially proposed for the h.c.p. case by Wilson (Edwards & Lipson, 1942; Wilson, 1942), this idea was then extended to the f.c.c. case (Paterson, 1952; Gevers, 1954*a*,*b*; Warren, 1959, 1963). More recently, Estevez-Rams *et al.* (2003, 2008) improved the accuracy and extended the validity range by including all terms in the stacking probability formulae, whereas Velterop *et al.* (2000) corrected the formalism to properly take the various *hkl* components of a peak into account.

In an f.c.c. system, reliable information can be obtained up to a few per cent of faults on the {111} plane. The trick is to describe the lattice with hexagonal axes, effectively transforming the problem into that of ⟨001⟩ stacking on the {111} plane. Under these hypotheses, the average phase term due to faulting can be written as

$$\left\langle \exp\left[2\pi i\varphi(L; d^*_{\{hkl\}}, L_0/h_0^2)\right]\right\rangle = A^F_{hkl}(L) + iB^F_{hkl}(L), \qquad (3.6.45)$$

where $L_0 = h + k + l$ and $h_0^2 = h^2 + k^2 + l^2$. The lattice symmetry influences the definitions of these two parameters. Faulting is one of the typical cases where a complex (sine) term is present, as peak shift and asymmetry in the profiles is expected (unless twin faults are absent). Following the treatment of Warren (see, for example, Warren, 1963), a set of recurrence equations can be written for the probability of the occurrence of faulting. The solution of the recurrence equations is used to generate the Fourier coefficients for faulting. In particular, if the probabilities of deformation and twin fault are α and β, respectively, then

$$S^2 = 3 - 12\alpha - 6\beta + 12\alpha^2 - \beta^2 + 24\alpha\beta(1-\alpha),$$
$$Z = \sqrt{(1-\beta^2) + S^2}/2 \qquad (3.6.46)$$

and, introducing the sign function,

$$\sigma_{L_0} = \begin{cases} +1 & \text{for } L_0 = 3N+1 \\ 0 & \text{for } L_0 = 3N \\ -1 & \text{for } L_0 = 3N-1 \end{cases} \qquad N = 0, \pm1, \pm2, \ldots, \qquad (3.6.47)$$

the Fourier coefficients can be obtained as

$$A^F_{hkl}(L) = \exp\left[\tfrac{1}{2}\ln(Z)|Ld^*_{\{hkl\}}\sigma_{L_0}L_0/h_0^2|\right], \qquad (3.6.48)$$

$$B^F_{hkl}(L) = -\sigma_{L_0}\frac{L}{|L|}\frac{L_0}{|L_0|}\frac{\beta}{S}A^F_{hkl}(L). \qquad (3.6.49)$$

Besides being asymmetric, each profile subcomponent can also be shifted with respect to the average Bragg position. For the subcomponent *hkl* the shift is

$$\delta_{hkl} = -\left[\frac{1}{2\pi}\arctan\left(\frac{s}{1-\beta}\right) - \frac{1}{6}\right]d^*_{\{hkl\}}\frac{L_0}{h_0^2}\sigma_{L_0}. \qquad (3.6.50)$$

In a given reflection family {*hkl*}, reflections affected and unaffected by faulting coexist, leading to peculiar shapes of the corresponding peak profiles.

Analogous formulae can be obtained for the b.c.c. and h.c.p. cases. In the former, the selection rule becomes $L_0 = -h - k + 2l$, whereas for the latter $L_0 = l$ and the condition for faulting is based on $h - k = 3N \pm 1$. Implementation requires the application of the proper formula to the particular reflection *hkl* considered in the analysis.

Analysing faults by observing just the peak shift, as in the original treatment of Warren (1959, 1963) or within the Warren–Averbach method (Warren & Averbach, 1950, 1952), would be erroneous, as it does not take the fine details of the broadening into account.

An alternative to the adoption of Warren's formalism was proposed by Balogh *et al.* (2006). Instead of performing the calculation explicitly, the authors parameterized the profiles obtained from the *DIFFaX* software (Treacy *et al.*, 1991) calculated for increasing quantities of faulting. The *DIFFaX* software is based on a recursive description of the stacking: the intensity is calculated along rods in reciprocal space using the tangent cylinder approximation. The parameterization, which is performed in terms of a sum of Lorentzian curves, is then employed for the evaluation of the fault-broadening profile at any angle. The modelling should be performed on a profile that contains a faulting-only contribution: note that for high faulting probabilities, it becomes arbitrary whether to assign the diffuse scattering part to one or another Bragg reflection. This introduces some arbitrariness in the subsequent (directional) convolution of the faulting profile with the other broadening effects. When applicable, however, this parameterization has several advantages: it takes the actual shape of the reciprocal-space rods into account (in an effective way), it does not necessitate any *hkl* selection rule and an analytical treatment can be employed, as the Lorentzian has an analytical transform. With the above caveats, it is in principle not even necessary to decompose the *DIFFaX*-generated profile if a numerical convolution is employed. This would also correspond to an extension of WPPM to the *DIFFaX*+ idea (Leoni, Gualtieri & Roveri, 2004; Leoni, 2008), or *vice versa*, where *DIFFaX*+ uses a corrected and improved version of the recursive approach of *DIFFaX* to

generate the profiles, but allows the refinement of all model parameters. [*DIFFaX+* is available from the author (matteo.leoni@unitn.it) on request.]

3.6.2.6.8. *Antiphase domain boundaries*

In the diffraction pattern of an ordered alloy, a dissimilar broadening can often be observed for structure and superstructure peaks (with the former being present in both the ordered and disordered states). The superstructure peaks, in fact, bear microstructural information on the interface between the ordered regions in the material: broadening occurs when domains meet out of phase, creating an antiphase domain boundary (APB or APDB). A general formula for APDB-related broadening does not exist: for a given ordered structure, the Fourier coefficients correspond to the normalized value of $A_{\mathrm{APDB},hkl}(L) = \overline{F(0)F^*(L)}$, where $F(0)$ is the structure factor of a cell positioned at $L = 0$ and $F^*(L)$ is the complex conjugate of the structure factor of a cell at a distance L along the direction $[hkl]$. Being the result of a combination of probabilities, the peak is always expected to be Lorentzian.

Explicit formulae have been derived for the Cu_3Au ordered alloy ($L1_2$ phase; Wilson, 1943; Wilson & Zsoldos, 1966; Scardi & Leoni, 2005). Several types of boundaries can form, depending on the way that the domains meet: the broadening depends both on the boundary plane and on the local arrangement of Au atoms leading to conservative (no Au atoms in contact) or nonconservative (Au atoms in contact) boundaries. By arranging the indices in such a way that $h \geq k \geq l$ and that l is always the unpaired index, the broadening of the superstructure reflections can be described as (Scardi & Leoni, 2005)

$$A^{\mathrm{APDB}}(L) = \exp[-2L\delta f(h, k, l)]. \tag{3.6.51}$$

In this formula, $\delta = \gamma_{\mathrm{APDB}}/a_0$ is the probability of occurrence of an APDB, a_0 is the unit-cell parameter and $f(h, k, l)$ is a function of hkl defined in Table 3.6.2, obtained from the results of Wilson (1943) and Wilson & Zsoldos (1966).

The average distance between two APDBs is given by $1/\delta$. For a random distribution of faults, the broadening is Lorentzian and $A^{\mathrm{APDB}} = \exp(-4L\delta/3)$.

3.6.2.7. *Assembling the equations into a peak and modelling the data*

As previously mentioned, the broadening contributions briefly illustrated in the previous sections are employed to generate the powder peak profile for reflections from the set of planes $\{hkl\}$ using equations (3.6.11) and (3.6.12) and where

$$\begin{aligned} I_{hkl}(s) &= k(d^*) \int_{-\infty}^{\infty} C(L)\exp(2\pi iLs)\,\mathrm{d}L \\ &= k(s) \int_{-\infty}^{\infty} T_{\mathrm{pV}}^{\mathrm{IP}}(L)A_{hkl}^{S}(L)[A_{hkl}^{D}(L)\cos(2\pi Ls) + iB_{hkl}^{D}(L)\sin(2\pi Ls)] \\ &\quad \times \ldots \times [A_{hkl}^{F}(L)\cos(2\pi Ls) + iB_{hkl}^{F}(L)\sin(2\pi Ls)]\,\mathrm{d}L. \end{aligned} \tag{3.6.52}$$

Table 3.6.2
Models for antiphase domain boundaries for the Cu_3Au case
$N = h^2 + k^2 + l^2$.

ID	Model	$f(h, k, l)$
1	Random	2/3
2	{100} planes	$\frac{2}{3}\frac{h+k+l}{\sqrt{N}}$
2.I	{100} planes, no Au–Au contacts	$(k+l)/\sqrt{N}$ if h is the unpaired index $(h+l)/\sqrt{N}$ if k is the unpaired index $(h+k)/\sqrt{N}$ if l is the unpaired index
2.II	{100} planes, only Au–Au contacts	$\frac{2h+k+l}{2\sqrt{N}}$ if h is the unpaired index $\frac{h+2k+l}{2\sqrt{N}}$ if k is the unpaired index $\frac{h+k+2l}{2\sqrt{N}}$ if l is the unpaired index
3	{110} planes	$\frac{2}{3}\frac{4h+2k}{\sqrt{2N}}$
3.I	{110} planes, Au displacement parallel or perpendicular to plane normal	$\frac{4h}{\sqrt{2N}}$ if h is the unpaired index $\frac{2h+2k}{\sqrt{2N}}$ otherwise
3.II	{110} planes, Au displacement at 60° to plane normal	$\frac{2h+2k}{\sqrt{2N}}$ if h is the unpaired index $\frac{3h+k}{\sqrt{2N}}$ otherwise
4	{111} planes	$\frac{8h}{3\sqrt{3N}}$ if $h \geq (k+l)$ $\frac{4(h+k+l)}{3\sqrt{3N}}$ otherwise

Equation (3.6.52) represents an asymmetrical peak profile (the asymmetry is given by the sine terms). Fast Fourier transform and space remapping (usually s to 2θ) are then employed to generate the peaks in the measurement space; intensities are multiplied by the Lorentz and, if needed, polarization terms, and a background is added to the whole pattern. Other aberrations (affecting the position, the intensity or the shape of the peak) can be included as needed.

The various reflections are then positioned on the basis of the (reference) Bragg angle $2\theta_B$ calculated from the unit-cell parameters, and a background (for example, a Chebychev polynomial) is suitably added. For completeness, thermal diffuse scattering should be included, as it can contribute to the broadening near the peak tails (see, for example, Beyerlein *et al.*, 2012). In addition, small-angle scattering can be considered to improve the WPPM result and to account for the observed increase in the background at low angle (Scardi *et al.*, 2011). The final equation is thus similar to that of the Rietveld (1969) or the Pawley (1981) methods,

$$I(2\theta) = \text{SAXS} + \text{TDS} + \text{bkg} + k(2\theta)LP\sum_{hkl} I_{\{hkl\}}(x), \quad (3.6.53)$$

the main difference being in the focus of the analysis and in the way that the profiles are generated.

The model parameters are then refined using a nonlinear least-squares routine (*e.g.* based on the Marquardt algorithm or suitable modifications, as proposed, for example, by Coelho, 2005) to directly match the synthesized pattern to the experimental data. The usual weight, related to Poisson counting statistics, is employed.

As the shape of each peak is bound to the underlying physical models, the number of parameters to be refined is usually quite limited. Compared with the four parameters per peak (intensity, width, shape and position) necessary for a Scherrer-type analysis, in WPPM we refine, for example, two parameters for a domain-size distribution, three parameters for dislocations (ρ, R_e' and φ), two parameters for faulting (α and β), at most six lattice parameters, a few background parameters (*e.g.* four parameters) and one parameter (intensity) per peak. In addition, we can also refine some further specimen-related parameters such as a misalignment error. No atomic coordinates are involved.

A flexible software package implementing WPPM (*PM2K*: Leoni *et al.*, 2006) is available from the author on request (matteo.leoni@unitn.it): the software includes all of the broadening models illustrated here. The user can work with any type and any simultaneous set of diffraction data (X-ray, neutrons or electrons) and build their own model with no *a priori* restriction on the quantity and type of parameters, the number of phases, the models or the relationships between the parameters. The WPPM method has also been implemented in the *TOPAS* refinement software [version 5 (Coelho, 2009; Bruker, 2009)] using the flexible macro language provided.[1]

3.6.2.7.1. *Alternative approaches*

Convolutional multiple whole profile fitting (CMWP; Ribárik *et al.*, 2004) and extended convolutional multiple whole profile fitting (eCMWP; Balogh *et al.*, 2006) have been developed to solve the same problem.

CMWP, introduced as a convolutive version of multiple whole profile fitting (MWP; Ungár *et al.*, 2001; Ribárik, 2008), is very similar to the WPPM. The notable differences are:

(i) The instrumental profile is employed directly without interpolation and the profile of the instrumental peak closest to the peak under analysis is used. The instrumental profile imposes conditions on the range of L used in profile modelling.

(ii) In CMWP a subset of data points is used for speed.

(iii) The background is given by the user (as a spline or Legendre polynomial).

(iv) All points of a given (generated) peak are weighted by the same value related to the maximum intensity. However, the correct weighting scheme with individual weights for data points is available as an option.

The authors also suggest using the MWP procedure in other cases, for example separately measured profiles or single crystals. The MWP procedure works in Fourier space so there is no direct possibility of checking the agreement between the model and data.

In the extended version (Balogh *et al.*, 2006), (e)CMWP introduces an interesting model for faults based on a parameterization of the profiles simulated with the *DIFFaX* software (Treacy *et al.*, 1991). This simulates the diffraction pattern of a faulted structure within the tangent cylinder approximation. The proposed parameterization allows more complex faulting models, at the expense of the calculation and parameterization of the profiles for any new, intermediate or mixed case or for any peak lying outside the parameterized range. The application of (e)CMWP is limited to cubic, hexagonal and orthorhombic powders with spherical or ellipsoidal domain shapes and assumes the presence of dislocations and faults.

It is worth mentioning two more alternative approaches: the Debye scattering equation (Debye, 1915; for some applications, see, for example, Cervellino *et al.*, 2003; Cozzoli *et al.*, 2006) and the total scattering (TS) approach [also known as pair distribution function (PDF) analysis; Egami & Billinge, 2003; Billinge, 2008; see also Chapter 5.7]. Both techniques work in real space: the first creates the pattern directly from atomic positions and the other extracts the real-space information (the PDF) from the diffraction data. As the information content does not change on moving from reciprocal (measured) to direct space, provided that similar hypotheses are employed (similar microstructure and, if necessary, structure), real-space and reciprocal-space methods should give similar results. Of course there are differences, related to the way that the data are handled. For instance, it is easier to visualize the anisotropic effects in reciprocal space, as the information is contained in the peak broadening (different peaks show different breadths): in the PDF this information is sparser as it should be reflected in a variation in the correlation lengths, but also (highly integrated) in a variation of the decay of the curve. Conversely, information on the atomic arrangement (*i.e.* on possible defects) appears more clearly in the PDF, where variations in the distances and in coordination are well localized, contrary to the diffraction pattern, where the information is contained in the (weak) diffuse signal, in the broadening and in the peak position.

Direct-space and reciprocal-space methods thus each have their own advantages and disadvantages. Combined or comparative modelling, whenever possible, is therefore always the best solution: we can match the flexibility and immediacy

[1] Some small errors are present in some versions of the WPPM macros implemented in *TOPAS*. An example of a corrected macro for a lognormal distribution of spheres is given in the supporting information. The implementation using the mean and variance of the distribution *versus* the lognormal mean and variance is straightforward. Please refer to Chapter 5.1 for corrected versions of the Fourier coefficients and ancillary equations that should be present in the macros.

of a real-space approach with the possibility of working directly with the measured data as typical in reciprocal-space methods.

3.6.3. Examples of WPPM analysis

To illustrate the power of the WPPM approach, a few examples are provided based both on simulated and on real data. The analyses were performed using the *PM2K* software (Leoni *et al.*, 2006). Similar results are obtained using the WPPM implementation in the commercial program *TOPAS*.

3.6.3.1. *Nanocrystalline ceria*

The first example concerns a nanocrystalline ceria powder obtained by the calcination of a cerium isopropoxide gel (Leoni, Di Maggio *et al.*, 2004; Leoni & Scardi, 2004; Scardi *et al.*, 2004). A large amount of XRD and transmisson electron microscopy (TEM) data have been collected on the same system (and specimen), starting from the xerogel and following calcination (Scardi *et al.*, 2010). Fig. 3.6.1(*a*) shows the X-ray powder diffraction pattern of the gel calcined for 1 h at 673 K measured with Cu radiation (40 kV, 45 mA) on a Rigaku PMG/VH diffractometer.

The data were collected over the 2θ range 18–154° (with a step of 0.05°) with a counting time of 60 s per step: a wide angular range and a high signal-to-noise ratio (SNR) are prerequisites for a proper line-profile analysis. The large span in reciprocal space is important for the complete characterization of any anisotropy in the broadening (a large set of independent directions in reciprocal space needs to be sampled), whereas the high SNR guarantees the collection of data at peak tails where the differences between similar microstructure models manifest themselves. The log scale employed in Fig. 3.6.1(*a*) highlights the low level of noise present in the pattern.

The diffractometer had 0.5° divergence and 2° Soller slits mounted on the primary arm and 0.15 mm antiscatter, 0.5° receiving and 2° Soller slits and a curved graphite analyzer crystal mounted on the secondary arm. This setup provided a narrow and symmetrical instrumental profile that could be described by a pseudo-Voigt curve and was thus ideal for line-profile analysis studies. The Caglioti *et al.* (1958) parameterization of the instrumental profile [*cf.* equations (3.6.18) and (3.6.19)] performed on the profiles of the NIST SRM 660a standard (LaB_6) is shown in Fig. 3.6.2.

Analysis of the pattern using traditional methods (see Scardi *et al.*, 2004) required 59 parameters, 53 of which were actually refined:

(i) one unit-cell parameter (a_0),
(ii) six (fixed) parameters defining the instrumental contribution [five parameters for the Caglioti parameterization (U, V, W, a and b) and one for the $K\alpha_2$ intensity ratio],
(iii) three parameters for the background,
(iv) one parameter for the specimen displacement,
(v) 48 parameters for the peaks (intensity, FWHM and shape for 16 peaks).

An analysis using traditional analysis methods resulted in an 'average domain size' of 3.65 (10) nm using the (modified) Warren–Averbach method and in the range from 4.95 (10) to 5.3 (1) nm using a (modified) Williamson–Hall approach. A discussion of the meaning and accuracy of the results can be found in Scardi *et al.* (2004).

The WPPM result, shown in Fig. 3.6.1(*b*), matches the experiment quite well: this is remarkable considering that the whole pattern (1800 data points) is modelled using just 32 parameters (26 free parameters):

(i) one unit-cell parameter (a_0),
(ii) six (fixed) parameters defining the instrumental contribution [five parameters for the Caglioti parameterization (U, V, W, a and b) and one for the $K\alpha_2$ intensity ratio],

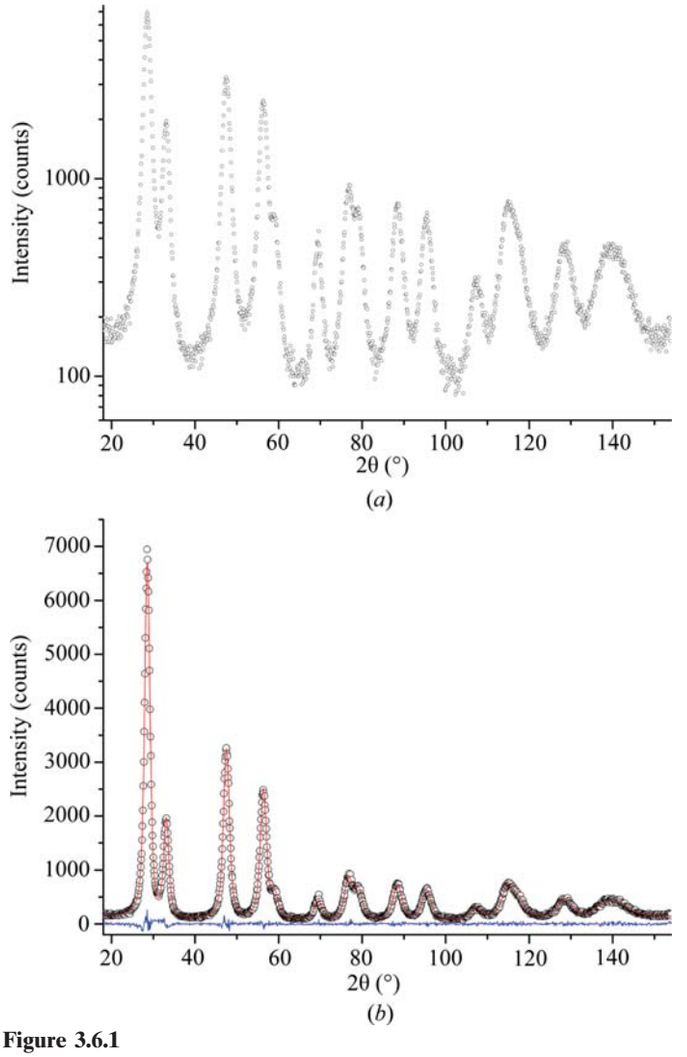

Figure 3.6.1
X-ray powder diffraction pattern of nanocrystalline ceria calcined at 673 K. In (*a*) the pattern is shown on a log scale to highlight the weak features in the data. In (*b*) the results of WPPM are shown: raw data (dots), model (line) and difference (lower line).

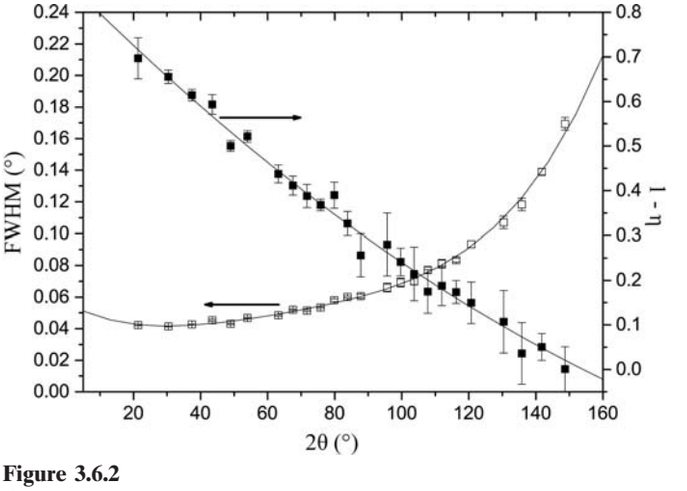

Figure 3.6.2
Parameterization of the instrumental resolution function using a pseudo-Voigt and the relationship of Caglioti *et al.* (1958).

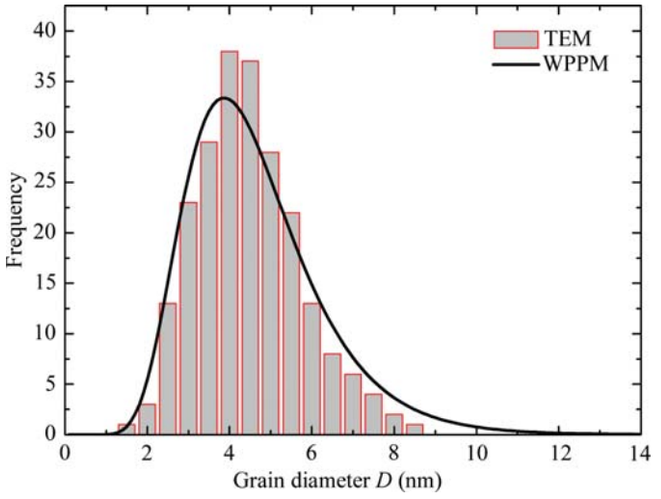

Figure 3.6.3
Size distribution of the ceria powder: WPPM (line) and TEM (histogram).

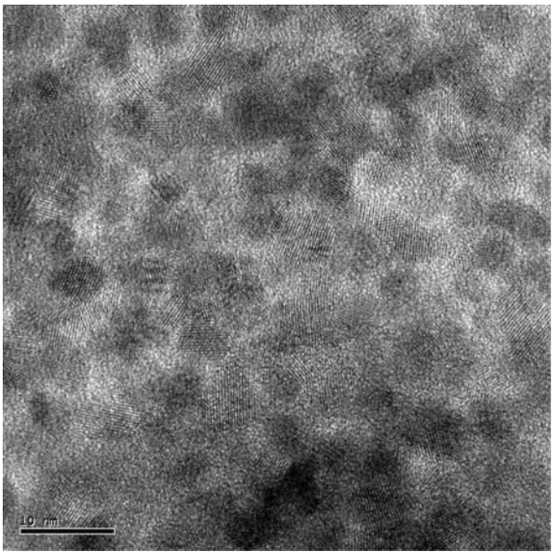

Figure 3.6.4
TEM micrograph of the calcined ceria powder. The scale bar represents 10 nm.

(iii) two parameters for the log-normal size distribution (μ and σ),
(iv) three parameters for the dislocation contributions (ρ, R_e and the mixing parameter f_e),
(v) three parameters for the background,
(vi) one parameter for the specimen displacement,
(vii) 16 parameters for the intensity of the peaks.

It is therefore possible to obtain more complete results with a number of parameters that is dramatically lower than that needed for the traditional analysis: the shapes of the peaks are interlinked *via* the microstructure models. It is suggested that the parameters are initialized with values providing a minimal but measurable effect (*i.e.*, for instance, $\mu = 2$, $\sigma = 0.4$, $\rho = 10^{15}$ m^{-2}, $f_e = 0.5$) to favour a rapid convergence.

By way of a check, Fig. 3.6.3 shows the good agreement between the size distribution obtained by WPPM and that obtained on the same specimen from the analysis of a large set of TEM micrographs (800 grains surveyed; Fig. 3.6.4). The data were collected on a 300 kV JEOL 3010 microscope (0.17 nm point-to-point resolution) equipped with a Gatan slow-scan 974 CCD camera (Leoni, Di Maggio *et al.*, 2004). Even if the particles are well separated, the analysis is quite tedious and prone to bias from the operator. The large and small particles are in fact easily missed, and overlapping particles are hard to separate and are usually not considered. Moreover, only the cross section is measured, as the transverse direction is difficult to access.

The statistical validity of the WPPM result is quite clear: a few million grains are probed by the X-rays *versus* the few hundred actually considered in microscopy. The WPPM result allows not only the mean (first moment) and variance to be obtained from the refined size distribution, but also the recovery of the most probable values for the traditional results (we know the shape and we can weight the column-length distribution by the surface or by the volume). In this case the numerical mean is ~4.3 nm: we can immediately understand the risk of placing faith in the results of a traditional analysis. The agreement between TEM and XRD is in any case excellent. The residual differences may be due both to the issues related to sizing under the microscope and to the simplified treatment employed in the WPPM (perfectly spherical domains, monodisperse shape, absence of surface relaxation *etc.*). A more complex model (accounting, for example, for surface relaxation effects) can be considered (see Scardi & Leoni, 2002; Leoni & Scardi, 2004), but the effects on the distribution are minimal.

The possibility of extracting information on the type of defects (*e.g.* dislocations, faults and APDBs) and on their amount is definitely a major advantage of WPPM over traditional methods and over TEM. For the determination of the dislocation density, the average contrast factor is needed; the actual expressions can be readily obtained from the single-crystal elastic constants (c_{11} = 403, c_{12} = 105 and c_{44} = 60 GPa; Nakajima *et al.*, 1994) as

$$\overline{C}_{\mathrm{CeO_2},e} = 0.122945 + 0.358092\frac{h^2k^2 + k^2l^2 + h^2l^2}{(h^2 + k^2 + l^2)^2}, \qquad (3.6.54)$$

$$\overline{C}_{\mathrm{CeO_2},s} = 0.105762 + 0.207999\frac{h^2k^2 + k^2l^2 + h^2l^2}{(h^2 + k^2 + l^2)^2} \qquad (3.6.55)$$

for edge and screw dislocations, respectively.

A dislocation density of 1.4×10^{16} m^{-2} was obtained for the specimen analysed here. This dislocation density immediately appears to be quite high when compared with the number of dislocations that can be identified in high-resolution TEM micrographs, as it corresponds to approximately one dislocation every couple of grains (Leoni & Scardi, 2004). However, the dislocations visible in the micrographs are just a small fraction of the total: if a dislocation is not properly aligned with the zone axis, it is in fact invisible (its presence can only be inferred from the effects of the distortion field). It is true that a sufficiently large number of dislocations must be present in order to give appreciable effects on the diffraction pattern, and TEM is still the better technique if the density of dislocations is below, for example, 10^{14} m^{-2}.

3.6.3.2. *Copper oxide*

The true power of WPPM, and of diffraction in general, can be appreciated in multi-phase systems. The unequivocal assignment of a structure to each grain is definitely impossible using TEM, unless each grain is individually sampled and carefully analysed. It is therefore quite hard to identify the phases present in the specimen and to characterize their microstructure independently from a micrograph alone. Conversely, information on the various phases is well separated in a diffraction pattern. The various (known) phases in a specimen can easily be identified (for

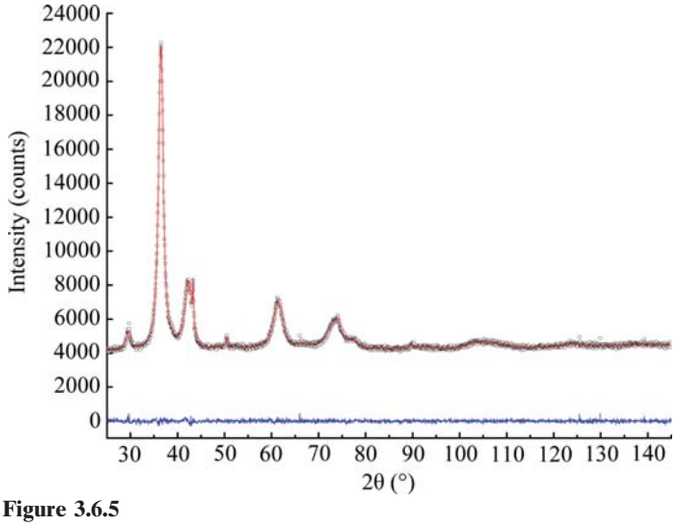

Figure 3.6.5
Result of WPPM of ball-milled Cu_2O: raw data (dots), model (line) and difference (lower line).

example by search/match in a large database such as the ICDD Powder Diffraction File): each diffraction peak belongs to a well defined phase and bears information on the microstructure of that phase.

As an example, Fig. 3.6.5 shows the diffraction pattern of a Cu_2O powder specimen obtained by grinding commercial Cu_2O powder (Carlo Erba) in a high-energy shatter mill (Fritsch Pulverisette 9). To limit the heating of the cup that would lead to dynamic recrystallization, milling was performed in 30 steps consisting of 10 s milling followed by 120 s room-temperature cooling (Martinez-Garcia *et al.*, 2007). The powder diffraction pattern was collected on the same diffractometer that was used for the analysis of the ceria powder. To obtain a sufficient SNR, the data were collected in the 18–154° 2θ range with a step size of 0.1° and a fixed acquisition time of 150 s per point. The fluorescence of the Cu present in the specimen is responsible for the large background that was not eliminated by the crystal analyser. From a quick comparison of Figs. 3.6.5 and 3.6.1, we notice a large difference at high angle: high strain effects (due to dislocations) are expected in this specimen as an effect of the extensive cold-work deformation introduced by the milling process.

A search match signals the presence of not just Cu_2O (cuprite, $Pn\bar{3}m$) but also metallic Cu (f.c.c. copper, $Fm\bar{3}m$) and CuO (tenorite, Cc) as minor phases, presumably due to reduction of the higher oxide. WPPM of the diffraction pattern, performed by considering all three observed phases, shows a flat residual (see Fig. 3.6.5). The severe peak overlap and the large broadening at high angle do not help in the analysis: the intensities of tenorite peaks (minor and broadened phase) were then constrained by a structural model (only a scale parameter was refined). Atomic coordinates and Debye–Waller factors for CuO were taken from the ICSD file (FIZ#69094; Brese *et al.*, 1990) and were considered to be constant.

Spherical domains were chosen for all phases. A log-normal distribution was used to model the minor phases. A histogram distribution was chosen for cuprite instead: the peaks clearly have a peculiar shape with a rather sharp tip, possibly indicating a wide, bimodal or odd size distribution (Leoni & Scardi, 2004). The size distribution resulting from the WPPM analysis is shown in Fig. 3.6.6(a): in this case it would be impossible for a traditional method to provide a physically sound result. The breadth of the profile is not fully informative: as the diffraction signal is proportional to the volume of matter, the actual distribution

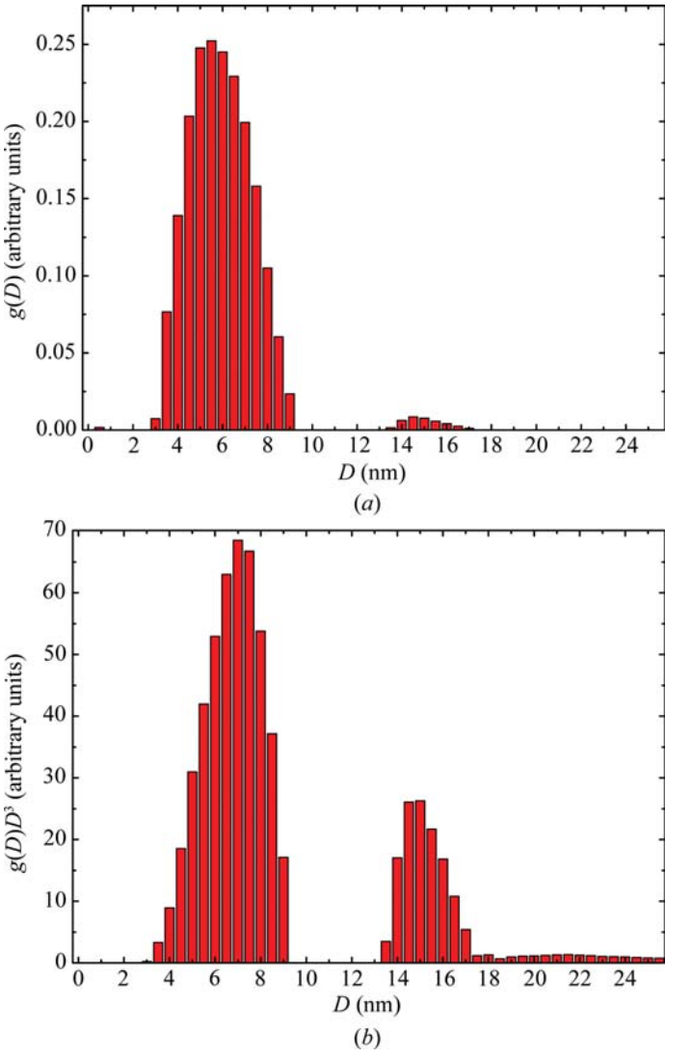

Figure 3.6.6
Domain-size distribution of cuprite: (a) WPPM result and (b) distribution multiplied by D^3.

'seen' in the experiment is that of Fig. 3.6.6(b), obtained by multiplying the result of Fig. 3.6.5(a) by D^3.

The larger size fraction therefore makes a non-negligible contribution to the pattern: as a rule of thumb, the smaller the domains and the wider the distribution, the stronger the contribution of the large domains. This problem of 'visibility' of small domains is attenuated when an analytical distribution (*e.g.* a log normal) can be used as the function goes smoothly to zero at zero size.

Dislocations can also be observed in these specimens: their quantification by TEM is nearly impossible due to the high defect density. The anisotropy term, *i.e.* the average contrast factor, has to be calculated for each of the three phases (Scardi *et al.*, 2007).

The slip system for Cu (c_{11} = 169, c_{12} =122, c_{44} = 75.3 GPa; Every & McCurdy, 1992a) is $\frac{1}{2}\langle 1\bar{1}0\rangle\{111\}$ and the corresponding average contrast factor (for edge and screw dislocations, respectively), is

$$\overline{C}_{\mathrm{Cu},e} = 0.304062 - 0.500211\,\frac{h^2k^2 + k^2l^2 + h^2l^2}{(h^2 + k^2 + l^2)^2}, \qquad (3.6.56)$$

$$\overline{C}_{\mathrm{Cu},s} = 0.298340 - 0.708805\,\frac{h^2k^2 + k^2l^2 + h^2l^2}{(h^2 + k^2 + l^2)^2}. \qquad (3.6.57)$$

For cuprite, the literature (Tromans & Meech, 2001) suggests that the main slip system is ⟨001⟩{100}. The contrast factor can be calculated analytically from the single-crystal elastic constants of cuprite (c_{11} = 121, c_{12} = 105 and c_{44} = 12.1 GPa; Every & McCurdy, 1992*b*) following Martinez-Garcia *et al.* (2007):

$$\overline{C}_{\mathrm{Cu_2O},e} = 0.355963 - 0.609491\,\frac{h^2k^2 + k^2l^2 + h^2l^2}{(h^2 + k^2 + l^2)^2}, \quad (3.6.58)$$

$$\overline{C}_{\mathrm{Cu_2O},s} = \frac{2}{3}\frac{h^2k^2 + k^2l^2 + h^2l^2}{(h^2 + k^2 + l^2)^2}. \quad (3.6.59)$$

For tenorite, a different approach was followed. The phase is minor and the single-crystal elastic constants are not readily available: we can therefore use the contrast factor in an effective way by refining the coefficients of the corresponding invariant [see equation (3.6.42)]. This preserves the profile shape determined by Wilkens' theory and just dilutes the meaning of the dislocation density. The average contrast factor is

$$\begin{aligned}\overline{C}_{\mathrm{CuO},\{hkl\}} &= \Big\{4\big[E_1h^4 + E_2k^4 + E_3l^4 + 2(E_4h^2k^2 + E_5k^2l^2 + E_6h^2l^2) \\ &\quad + 4(E_7h^3k + E_8h^3l + E_9k^3h)\big]Y^4Z^4\sin^4\beta\Big\} \\ &\quad \times \Big(\big\{k^2Z^2 + 2Y^2(l^2 + h^2Z^2) - Z[4hlY^2\cos(\beta) + k^2Z\cos(2\beta)]\big\}^2\Big)^{-1}, \end{aligned} \quad (3.6.60)$$

where a, b, c and β are the unit-cell parameters of tenorite, $Y = b/a$ and $Z = c/a$.

The dislocation density in Cu_2O is quite high [ρ = 2.8 (5) × 10^{16} m^{-2}]: dislocations are more of the edge character [f_E = 0.85 (3)] and the outer cutoff radius R_e = 9 (3) nm leads to a Wilkens' parameter of approximately 1.5, suggesting a strong dislocation interaction. The high dislocation density in this material is justified by the very low shear modulus (G = 10.3 GPa; Every & McCurdy, 1992*b*), whereas the high dislocation interaction is the result of the severe deformation induced by the milling.

APPENDIX A3.6.1
Functions for profile shapes

The unit-area Gaussian $G(x, \omega)$ and Lorentzian $L(x, \omega)$ functions are defined as

$$G(x, \omega) = \frac{2\sqrt{\ln 2/\pi}}{\omega}\exp\left(-\frac{4x^2\ln 2}{\omega^2}\right), \quad (3.6.61)$$

$$L(x, \omega) = \frac{2}{\pi\omega}\left(\frac{1}{1 + 4x^2/\omega^2}\right), \quad (3.6.62)$$

where x is the running variable and ω is the full-width at half-maximum. Based on these definitions, the Voigt and pseudo-Voigt are

$$V(x, \omega_L, \omega_G) = L(x, \omega_L) \otimes G(x, \omega_G) \quad (3.6.63)$$

and

$$\mathrm{pV}(x, \omega_L, \omega_G) = \eta L(x, \omega_L) + (1 - \eta)G(x, \omega_G), \quad (3.6.64)$$

respectively, where η is the mixing parameter (ranging between 0 and 1) and w_L and w_G are the width of the Lorentzian and Gaussian components, respectively.

References

Adler, T. & Houska, C. R. (1979). *Simplifications in the X-ray line-shape analysis. J. Appl. Phys.* **50**, 3282–3287.

Alexander, L. (1954). *The synthesis of X-ray spectrometer line profiles with application to crystallite size measurements. J. Appl. Phys.* **25**, 155–161.

Armstrong, N., Leoni, M. & Scardi, P. (2006). *Considerations concerning Wilkens' theory of dislocation line-broadening. Z. Kristallogr. Suppl.* **23**, 81–86.

Balogh, L., Ribárik, G. & Ungár, T. (2006). *Stacking faults and twin boundaries in fcc crystals determined by X-ray diffraction profile analysis. J. Appl. Phys.* **100**, 023512.

Balzar, D. & Popović, S. (1996). *Reliability of the simplified integral-breadth methods in diffraction line-broadening analysis. J. Appl. Cryst.* **29**, 16–23.

Bergmann, J. & Kleeberg, R. (2001). *Fundamental parameters versus learnt profiles using the Rietveld program BGMN. Mater. Sci. Forum*, **378–381**, 30–37.

Berkum, J. G. M. van (1994). *Strain Fields in Crystalline Materials*. PhD thesis, Technische Universiteit Delft, Delft, The Netherlands.

Bertaut, E. F. (1949*a*). *Etude aux rayons X de la répartition des dimensions des cristallites dans une poudre cristalline. C. R. Acad. Sci.* **228**, 492–494.

Bertaut, E. F. (1949*b*). *Signification de la dimension cristalline mesurée d'apres la largeur de raie Debye-Scherrer. C. R. Acad. Sci.* **228**, 187–189.

Bertaut, E. F. (1950). *Raies de Debye–Scherrer et repartition des dimensions des domaines de Bragg dans les poudres polycristallines. Acta Cryst.* **3**, 14–18.

Beyerlein, K. R., Leoni, M. & Scardi, P. (2012). *Temperature diffuse scattering of nanocrystals. Acta Cryst.* A**68**, 382–392.

Billinge, S. J. L. (2008). *Local structure from total scattering and atomic pair distribution function (PDF) analysis.* In *Powder Diffraction: Theory and Practice*, edited by R. E. Dinnebier & S. J. L. Billinge. London: Royal Society of Chemistry.

Brese, N. E., O'Keeffe, M., Ramakrishna, B. L. & Von Dreele, R. B. (1990). *Low-temperature structures of CuO and AgO and their relationships to those of MgO and PdO. J. Solid State Chem.* **89**, 184–190.

Bruker (2009). *DIFFRAC.SUITE TOPAS*, *Total Pattern Analysis Solution.* Version 5. Bruker AXS, Karlsruhe, Germany.

Caglioti, G., Paoletti, A. & Ricci, F. P. (1958). *Choice of collimator for a crystal spectrometer for neutron diffraction. Nucl. Instrum.* **3**, 223–228.

Cervellino, A., Giannini, C. & Guagliardi, A. (2003). *Determination of nanoparticle structure type, size and strain distribution from X-ray data for monatomic f.c.c.-derived non-crystallographic nanoclusters. J. Appl. Cryst.* **36**, 1148–1158.

Cheary, R. W. & Coelho, A. (1992). *A fundamental parameters approach to X-ray line-profile fitting. J. Appl. Cryst.* **25**, 109–121.

Cheary, R. W. & Coelho, A. (1994). *Synthesizing and fitting linear position-sensitive detector step-scanned line profiles. J. Appl. Cryst.* **27**, 673–681.

Cheary, R. W. & Coelho, A. A. (1998*a*). *Axial divergence in a conventional X-ray powder diffractometer. I. Theoretical foundations. J. Appl. Cryst.* **31**, 851–861.

Cheary, R. W. & Coelho, A. A. (1998*b*). *Axial divergence in a conventional X-ray powder diffractometer. II. Realization and evaluation in a fundamental-parameter profile fitting procedure. J. Appl. Cryst.* **31**, 862–868.

Cline, J. P., Black, D., Windover, D. & Henins, A. (2010). *SRM 660b – Line Position and Line Shape Standard for Powder Diffraction.* https://www-s.nist.gov/srmors/view_detail.cfm?srm=660b.

Coelho, A. A. (2005). *A bound constrained conjugate gradient solution method as applied to crystallographic refinement problems. J. Appl. Cryst.* **38**, 455–461.

Coelho, A. A. (2009). *TOPAS Academic.* Version 5. http://www.topas-academic.net/.

Cozzoli, P. D., Snoeck, E., Garcia, M. A., Giannini, C., Guagliardi, A., Cervellino, A., Gozzo, F., Hernando, A., Achterhold, K., Ciobanu, N., Parak, F. G., Cingolani, R. & Manna, L. (2006). *Colloidal synthesis and characterization of tetrapod-shaped magnetic nanocrystals. Nano Lett.* **6**, 1966–1972.

Debye, P. (1915). *Zerstreuung von Röntgenstrahlen. Ann. Phys.* **351**, 809–823.

Deutsch, M., Forster, E., Holzer, G., Hartwig, J., Hämäläinen, K., Kao, C.-C., Huotari, S. & Diamant, R. (2004). *X-ray spectrometry of copper: new results on an old subject. J. Res. Natl Inst. Stand. Technol.* **109**, 75–98.

Dragomir, I. C. & Ungár, T. (2002). *Contrast factors of dislocations in the hexagonal crystal system. J. Appl. Cryst.* **35**, 556–564.

Drits, V. A. & Tchoubar, C. (1990). *X-ray Diffraction by Disordered Lamellar Structures: Theory and Applications to Microdivided Silicates and Carbons.* Berlin: Springer-Verlag.

Edwards, O. S. & Lipson, H. (1942). *Imperfections in the structure of cobalt. I. Experimental work and proposed structure. Proc. R. Soc. Lond. Ser. A*, **180**, 268–277.

Egami, T. & Billinge, S. J. L. (2003). *Underneath the Bragg Peaks. Structural Analysis of Complex Materials.* Oxford: Elsevier.

Estevez-Rams, E., Leoni, M., Scardi, P., Aragon-Fernandez, B. & Fuess, H. (2003). *On the powder diffraction pattern of crystals with stacking faults. Philos. Mag.* **83**, 4045–4057.

Estevez-Rams, E., Welzel, U., Pentón Madrigal, A. & Mittemeijer, E. J. (2008). *Stacking and twin faults in close-packed crystal structures: exact description of random faulting statistics for the full range of faulting probabilities. Acta Cryst.* A**64**, 537–548.

Every, A. G. & McCurdy, A. K. (1992*a*). *Landolt–Börnstein: Crystal and Solid State Physics New Series*, Group III, Vol. 29, edited by D. F. Nelson, p. 12. Berlin: Springer.

Every, A. G. & McCurdy, A. K. (1992*b*). *Landolt–Börnstein: Crystal and Solid State Physics New Series*, Group III, Vol. 29, edited by D. F. Nelson, p. 68. Berlin: Springer.

Garrod, R. I., Brett, J. F. & MacDonald, J. A. (1954). *X-ray line broadening and pure diffraction contours. Aust. J. Phys.* **7**, 77–95.

Gevers, R. (1954*a*). *X-ray diffraction by close-packed crystals with 'growth stacking faults' assuming an 'N-layer influence'. Acta Cryst.* **7**, 492–494.

Gevers, R. (1954*b*). *X-ray diffraction by close-packed crystals with 'growth-' and 'deformation or transformation stacking faults' assuming an 'N-layer influence'. Acta Cryst.* **7**, 740–744.

Grebille, D. & Bérar, J.-F. (1985). *Calculation of diffraction line profiles in the case of a major size effect: application to boehmite AlOOH. J. Appl. Cryst.* **18**, 301–307.

Groma, I., Ungár, T. & Wilkens, M. (1988). *Asymmetric X-ray line broadening of plastically deformed crystals. I. Theory. J. Appl. Cryst.* **21**, 47–54.

Hölzer, G., Fritsch, M., Deutsch, M., Härtwig, J. & Förster, E. (1997). *$K\alpha_{1,2}$ and $K\beta_{1,3}$ X-ray emission lines of the 3d transition metals. Phys. Rev. A*, **56**, 4554–4568.

Houska, C. R. & Smith, T. M. (1981). *Least-squares analysis of X-ray diffraction line shapes with analytic functions. J. Appl. Phys.* **52**, 748.

Jones, F. W. (1938). *The measurement of particle size by the X-ray method. Proc. R. Soc. Lond. Ser. A*, **166**, 16–43.

Kaganer, V. M. & Sabelfeld, K. K. (2010). *X-ray diffraction peaks from correlated dislocations: Monte Carlo study of dislocation screening. Acta Cryst.* A**66**, 703–716.

Kamminga, J.-D. & Delhez, R. (2000). *Calculation of diffraction line profiles from specimens with dislocations. A comparison of analytical models with computer simulations. J. Appl. Cryst.* **33**, 1122–1127.

Kern, A. A. & Coelho, A. A. (1998). *A new fundamental parameters approach in profile analysis of powder data.* New Delhi: Allied Publishers.

Klimanek, P. & Kuzel, R. (1988). *X-ray diffraction line broadening due to dislocations in non-cubic materials. I. General considerations and the case of elastic isotropy applied to hexagonal crystals. J. Appl. Cryst.* **21**, 59–66.

Klug, H. P. & Alexander, L. E. (1974). *X-ray Diffraction Procedures for Polycrystalline and Amorphous Materials*, 2nd ed. New York: Wiley.

Krill, C. E. & Birringer, R. (1998). *Estimating grain-size distributions in nanocrystalline materials from X-ray diffraction profile analysis. Philos. Mag. A*, **77**, 621–640.

Krivoglaz, M. A. (1969). *Theory of X-ray and Thermal Neutron Scattering by Real Crystals.* New York: Plenum Press.

Krivoglaz, M. A., Martynenko, O. V. & Ryaboshapka, K. P. (1983). *Influence of correlation in position of dislocations on X-ray diffraction by deformed crystals. Phys. Met. Metall.* **55**, 1–12.

Krivoglaz, M. A. & Ryaboshapka, K. P. (1963). *Theory of X-ray scattering by crystals containing dislocations. Screw and edge dislocations randomly distributed throughout the crystal. Phys. Met. Metall.* **15**, 14–26.

Kuzel, R. & Klimanek, P. (1989). *X-ray diffraction line broadening due to dislocations in non-cubic crystalline materials. III. Experimental results for plastically deformed zirconium. J. Appl. Cryst.* **22**, 299–307.

Langford, J. I. & Louër, D. (1982). *Diffraction line profiles and Scherrer constants for materials with cylindrical crystallites. J. Appl. Cryst.* **15**, 20–26.

Langford, J. I. & Wilson, A. J. C. (1978). *Scherrer after sixty years: a survey and some new results in the determination of crystallite size. J. Appl. Cryst.* **11**, 102–113.

Leineweber, A. (2011). *Understanding anisotropic microstrain broadening in Rietveld refinement. Z. Kristallogr.* **226**, 905–923.

Leineweber, A. & Mittemeijer, E. J. (2004). *Diffraction line broadening due to lattice-parameter variations caused by a spatially varying scalar variable: its orientation dependence caused by locally varying nitrogen content in ε-$FeN_{0.433}$. J. Appl. Cryst.* **37**, 123–135.

Leineweber, A. & Mittemeijer, E. J. (2010). *Notes on the order-of-reflection dependence of microstrain broadening. J. Appl. Cryst.* **43**, 981–989.

Lele, S. & Anantharaman, T. R. (1966). *Influence of crystallite shape on particle size broadening of Debye–Scherrer reflections. Proc. Indian Acad. Sci. A*, **64**, 261–274.

Leonardi, A., Leoni, M., Siboni, S. & Scardi, P. (2012). *Common volume functions and diffraction line profiles of polyhedral domains. J. Appl. Cryst.* **45**, 1162–1172.

Leoni, M. (2008). *Diffraction analysis of layer disorder. Z. Kristallogr.* **223**, 561–568.

Leoni, M., Confente, T. & Scardi, P. (2006). *PM2K: a flexible program implementing whole powder pattern modelling. Z. Kristallogr. Suppl.* **23**, 249–254.

Leoni, M., Di Maggio, R., Polizzi, S. & Scardi, P. (2004). *X-ray diffraction methodology for the microstructural analysis of nanocrystalline powders: application to cerium oxide. J. Am. Ceram. Soc.* **87**, 1133–1140.

Leoni, M., Gualtieri, A. F. & Roveri, N. (2004). *Simultaneous refinement of structure and microstructure of layered materials. J. Appl. Cryst.* **37**, 166–173.

Leoni, M., Martinez-Garcia, J. & Scardi, P. (2007). *Dislocation effects in powder diffraction. J. Appl. Cryst.* **40**, 719–724.

Leoni, M. & Scardi, P. (2004). *Nanocrystalline domain size distributions from powder diffraction data. J. Appl. Cryst.* **37**, 629–634.

Leoni, M., Scardi, P. & Langford, J. I. (1998). *Characterization of standard reference materials for obtaining instrumental line profiles. Powder Diffr.* **13**, 210–215.

Martinez-Garcia, J., Leoni, M. & Scardi, P. (2007). *Analytical expression for the dislocation contrast factor of the ⟨001⟩{100} cubic slip-system: Application to Cu_2O. Phys. Rev. B*, **76**, 174117.

Martinez-Garcia, J., Leoni, M. & Scardi, P. (2008). *Analytical contrast factor of dislocations along orthogonal diad axes. Philos. Mag. Lett.* **88**, 443–451.

Martinez-Garcia, J., Leoni, M. & Scardi, P. (2009). *A general approach for determining the diffraction contrast factor of straight-line dislocations. Acta Cryst.* A**65**, 109–119.

Matěj, Z., Matějová, L., Novotný, F., Drahokoupil, J. & Kuzel, R. (2011). *Determination of crystallite size distribution histogram in nanocrystalline anatase powders by XRD. Z. Kristallogr. Proc.* **1**, 87–92.

Nakajima, A., Yoshihara, A. & Ishigame, M. (1994). *Defect-induced Raman spectra in doped CeO_2. Phys. Rev. B*, **50**, 13297–13307.

Nye, J. F. (1987). *Physical Properties of Crystals: Their Representation by Tensors and Matrices*, reprint edition. Oxford University Press.

Paterson, M. S. (1952). *X-ray diffraction by face-centered cubic crystals with deformation faults. J. Appl. Phys.* **23**, 805–811.

Patterson, A. L. (1939). *The Scherrer formula for X-ray particle size determination. Phys. Rev.* **56**, 978–982.

Pawley, G. S. (1981). *Unit-cell refinement from powder diffraction scans. J. Appl. Cryst.* **14**, 357–361.

Popa, N. C. (1998). *The (hkl) dependence of diffraction-line broadening caused by strain and size for all Laue groups in Rietveld refinement. J. Appl. Cryst.* **31**, 176–180.

Rao, S. & Houska, C. R. (1986). *X-ray diffraction profiles described by refined analytical functions. Acta Cryst.* A**42**, 14–19.

Ribárik, G. (2008). *Modeling of Diffraction Patterns Properties.* PhD thesis, Eötvös University, Budapest.

Ribárik, G., Gubicza, J. & Ungár, T. (2004). *Correlation between strength and microstructure of ball-milled Al–Mg alloys determined by X-ray diffraction. Mater. Sci. Eng. A Struct. Mater.* **387–389**, 343–347.

Rietveld, H. M. (1969). *A profile refinement method for nuclear and magnetic structures. J. Appl. Cryst.* **2**, 65–71.

Scardi, P. & Leoni, M. (1999). *Fourier modelling of the anisotropic line broadening of X-ray diffraction profiles due to line and plane lattice defects. J. Appl. Cryst.* **32**, 671–682.

Scardi, P. & Leoni, M. (2001). *Diffraction line profiles from polydisperse crystalline systems. Acta Cryst.* A**57**, 604–613.

Scardi, P. & Leoni, M. (2002). *Whole powder pattern modelling. Acta Cryst.* A**58**, 190–200.

Scardi, P. & Leoni, M. (2004). *Whole powder pattern modelling: theory and application.* In *Diffraction Analysis of the Microstructure of Materials*, edited by E. J. Mittemeijer & P. Scardi, pp. 51–91. Berlin: Springer-Verlag.

Scardi, P. & Leoni, M. (2005). *Diffraction whole-pattern modelling study of anti-phase domains in Cu_3Au. Acta Mater.* **53**, 5229–5239.

Scardi, P., Leoni, M. & Beyerlein, K. R. (2011). *On the modelling of the powder pattern from a nanocrystalline material. Z. Kristallogr.* **226**, 924–933.

Scardi, P., Leoni, M. & Delhez, R. (2004). *Line broadening analysis using integral breadth methods: a critical review. J. Appl. Cryst.* **37**, 381–390.

Scardi, P., Leoni, M., Müller, M. & Di Maggio, R. (2010). *In situ size-strain analysis of nanocrystalline ceria growth. Mater. Sci. Eng. A Struct. Mater.* **528**, 77–82.

Scardi, P., Leoni, M., Straffelini, G. & Giudici, G. D. (2007). *Microstructure of Cu–Be alloy triboxidative wear debris. Acta Mater.* **55**, 2531–2538.

Scherrer, P. (1918). *Bestimmung der Grösse und der inneren Struktur von Kolloidteilchen mittels Röntgenstrahlen. Nachr. Ges. Wiss. Göttingen*, pp. 98–100.

Stephens, P. W. (1999). *Phenomenological model of anisotropic peak broadening in powder diffraction. J. Appl. Cryst.* **32**, 281–289.

Stokes, A. R. & Wilson, A. J. C. (1942). *A method of calculating the integral breadths of Debye–Scherrer lines. Math. Proc. Cambridge Philos. Soc.* **38**, 313–322.

Stokes, A. R. & Wilson, A. J. C. (1944). *The diffraction of X-rays by distorted crystal aggregates – I. Proc. Phys. Soc.* **56**, 174–181.

Treacy, M. M. J., Newsam, J. M. & Deem, M. W. (1991). *A general recursion method for calculating diffracted intensities from crystals containing planar faults. Proc. R. Soc. Lond. Ser. A*, **433**, 499–520.

Tromans, D. & Meech, J. A. (2001). *Enhanced dissolution of minerals: stored energy, amorphism and mechanical activation. Miner. Eng.* **14**, 1359–1377.

Ungár, T. (2001). *Dislocation densities, arrangements and character from X-ray diffraction experiments. Mater. Sci. Eng. A Struct. Mater.* **309–310**, 14–22.

Ungár, T. & Borbély, A. (1996). *The effect of dislocation contrast on X-ray line broadening: a new approach to line profile analysis. Appl. Phys. Lett.* **69**, 3173.

Ungár, T., Dragomir, I., Révész, Á. & Borbély, A. (1999). *The contrast factors of dislocations in cubic crystals: the dislocation model of strain anisotropy in practice. J. Appl. Cryst.* **32**, 992–1002.

Ungár, T., Gubicza, J., Ribárik, G. & Borbély, A. (2001). *Crystallite size distribution and dislocation structure determined by diffraction profile analysis: principles and practical application to cubic and hexagonal crystals. J. Appl. Cryst.* **34**, 298–310.

Ungár, T. & Tichy, G. (1999). *The effect of dislocation contrast on X-ray line profiles in untextured polycrystals. Phys. Stat. Solidi A Appl. Res.* **171**, 425–434.

Vargas, R., Louër, D. & Langford, J. I. (1983). *Diffraction line profiles and Scherrer constants for materials with hexagonal crystallites. J. Appl. Cryst.* **16**, 512–518.

Velterop, L., Delhez, R., de Keijser, Th. H., Mittemeijer, E. J. & Reefman, D. (2000). *X-ray diffraction analysis of stacking and twin faults in f.c.c. metals: a revision and allowance for texture and non-uniform fault probabilities. J. Appl. Cryst.* **33**, 296–306.

Warren, B. E. (1959). *X-ray studies of deformed metals. Progr. Met. Phys.* **8**, 147–202.

Warren, B. E. (1963). *Single- and double-deformation faults in face-centered cubic crystals. J. Appl. Phys.* **34**, 1973–1975.

Warren, B. E. (1990). *X-ray Diffraction.* New York: Dover Publications. (Unabridged reprint of the original 1969 book.)

Warren, B. E. & Averbach, B. L. (1950). *The effect of cold-work distortion on X-ray patterns. J. Appl. Phys.* **21**, 595–599.

Warren, B. E. & Averbach, B. L. (1952). *The separation of cold-work distortion and particle size broadening in X-ray patterns. J. Appl. Phys.* **23**, 492.

Welberry, T.R. (2004). *Diffuse X-ray Scattering and Models of Disorder.* Oxford University Press.

Wilkens, M. (1970*a*). *The determination of density and distribution of dislocations in deformed single crystals from broadened X-ray diffraction profiles. Phys. Stat. Solidi A Appl. Res.* **2**, 359–370.

Wilkens, M. (1970*b*). *Fundamental Aspects of Dislocation Theory*, edited by J. A. Simmons, R. de Wit & R. Bullough, Vol. II, pp. 1195–1221. Washington DC: National Institute of Standards and Technology.

Wilkens, M. (1987). *X-ray line broadening and mean square strains of straight dislocations in elastically anisotropic crystals of cubic symmetry. Phys. Stat. Solidi A Appl. Res.* **104**, K1–K6.

Williamson, G. K. & Hall, W. H. (1953). *X-ray line broadening from filed aluminium and wolfram. Acta Metall.* **1**, 22–31.

Wilson, A. J. C. (1942). *Imperfections in the structure of cobalt. II. Mathematical treatment of proposed structures. Proc. R. Soc. Lond. Ser. A*, **180**, 277–285.

Wilson, A. J. C. (1943). *The reflexion of X-rays from the 'anti-phase nuclei' of $AuCu_3$. Proc. R. Soc. Lond. Ser. A*, **181**, 360–368.

Wilson, A. J. C. (1963). *Mathematical Theory of X-ray Powder Diffractometry.* New York: Gordon & Breach.

Wilson, A. J. C. (1969). *Variance apparent particle sizes for cylinders, prisms and hemispheres. J. Appl. Cryst.* **2**, 181–183.

Wilson, A. J. C. & Zsoldos, L. (1966). *The reflexion of X-rays from the 'anti-phase nuclei' of $AuCu_3$. II. Proc. R. Soc. Lond. Ser. A*, **290**, 508–514.